and the parental cell (KP4) were used in all of the experiments. Selected clones were routinely maintained in DMEM containing 10% fetal bovine serum (JRH Biosciences, Lenexa, KS, U.S.A.) and 500 μg/ml Geneticin at 37°C in humidified air containing 5% CO_2.

To identify the localization of MnSOD and mito(−) MnSOD, KP4 cells were also transfected with pEGFP expression plasmid with the *MnSOD* gene or the *MnSOD* gene lacking MTS, which encodes the entire open reading frame of MnSOD or the MnSOD lacking a mitochondria targeting peptide, and also the mitochondria targeting peptide alone. To construct pEGFP expression plasmids, the cDNAs were incised with *Eco* RI and *Hind* III from the PCR products and inserted into the pEGFP-N1 expression vector (Clontech, San Diego, CA, U.S.A.). The construct was transformed into an XL1 Blue competent cell (Stratagene, La Jolla, CA, U.S.A.) and purified with a QIAFilter Plasmid Kit (QIAGEN, Valencia, CA, U.S.A.). The product was then transfected into cells using the GenePORTER 2 (Gene Therapy Systems), using the same method as described in the pCR3.1-Uni plasmid transfection procedure above. The transfected cells were visualized using a CSU-10 confocal laser scanning unit (Yokogawa Electric Co., Tokyo, Japan) coupled to an IX90 inverted microscope with a UPlanAPO X40 objective lens (Olympus Optical Co., Tokyo, Japan), and a C5810-01 color chilled 3CCD camera (Hamamatsu Photonics K. K., Hamamatsu, Japan). The cells were excited at 488 nm, and the emission was filtered using a 515-nm barrier filter. To ascertain localization of mitochondria, the cells were stained with MitoTracker Red CMXRos (Molecular Probes, Eugene, OR, U.S.A.), then visualized using a confocal laser scanning microscope excited at 488 nm, whereas the emission was filtered using a 580-nm barrier filter. A merged double image of (GFP) and MitoTracker was taken using a confocal laser scanning microscope excited at 488 nm, and the emission was filtered using a double-window barrier filter, of which the ranges were 510–590 and 580–620 nm.

In vitro *biological experimental system for hypoxia and PO_2 measurement system*

Biological experiments were performed in a hypoxic chamber [Anaerobic System MIP-1025 (Forma Scientific, Marietta, OH, U.S.A.)], which was specially modified to culture mammalian cells. The conditions inside the chamber were maintained with 95% humidified nitrogen plus 5% CO_2. The medium PO_2 in a representative flask was measured with MT 5000S (MTGiken, Tokyo, Japan), which was designed and made especially for our experimental system. This equipment included a small electrode (0.2 mm in diameter), which could detect PO_2 at a level as low as 0.1 mm Hg. A hypoxic condition of <8 mm Hg was maintained throughout the experiments. For H/R treatment, cells were maintained in hypoxia for 24 h followed by subsequent exposure to air.

Superoxide dismutase (SOD) activity gel assay

A nondenatured gel assay for SOD activity was performed according to a previously described method (3) with slight modifications. Cells were sonicated in a 50 m*M* potassium phosphate buffer (pH 7.8). Fifty micrograms of protein per lane was electrophoresed through a nondissociating riboflavin gel consisting of 5% stacking gel (pH 6.8) and 12% running gel (pH 8.8) at 4°C. To visualize SOD activity, gels were first incubated in 2.43 m*M* nitro blue tetrazolium (Wako Pure Chemical Industries, Ltd., Osaka, Japan) in deionized water for 20 min, and then in 0.028 m*M* riboflavin (Wako Pure Chemical Industries, Ltd.) and 280 m*M* TEMED (*N,N,N',N'*-tetramethyl ethylenediamine; Sigma Chemical Co., St. Louis, MO, U.S.A.) in a 50 m*M* potassium phosphate buffer (pH 7.8) for 15 min in the dark. Gels were then washed in deionized water and illuminated under a fluorescent light until clear zones of SOD activity were evident. The images were obtained as TIFF files by a CCD camera in connection with a Power Macintosh G4 (Apple Computer, Inc., Cupertino, CA, U.S.A.). The bands of MnSOD were quantified by NIH Image 1.61, which is available on the Internet via a file-transfer protocol from http://rsb.info.nih.gov/nih-image/download.html. The MnSOD activity of the parental cell was used as the reference, and the relative MnSOD activities of other cells were normalized to those in the parental cells. The mean of the integrated density obtained from three independent experiments was used as a representative value for the experiment.

RT-PCR detection in MnSOD cells and mito(−) cells

Total RNA was isolated from cultured cells using the acid guanidinium–phenol–chloroform method (9). First-strand cDNA was synthesized using Moloney leukemia virus reverse transcriptase (TOYOBO, Tokyo, Japan) with an antisense primer, MnGPB 5′ CCCGAATTCCCTTTTTGCAAGCCATGTATCT 3′. A subsequent PCR was then performed using the same antisense primer, MnGPB, and a sense primer, MnGPA 5′ GGGAAGCTTTGGCTTCGGCAGCGGCTTCAG 3′, which is for detecting a whole range of normal MnSOD mRNA, or a sense primer, Mnmt-GPA 5′ GGGAAGCTTATGAAGCACAGCCTCCCCGACCTG 3′, which is for detecting MnSOD lacking MTS mRNA, using ExTaq DNA polymerase (TaKaRa, Tokyo, Japan) (Fig. 1). PCR was conducted in a PerkinElmer Cetus Thermal Cycler for 31 cycles. After 5 min at 94°C and 5 min at 60°C, amplification was performed for a cycling profile consisting of extension at 72°C for 1 min, denaturation at 94°C for 30 s, and annealing at 60°C for 30 s, followed by final extension at 72°C for 10 min. The PCR products were analyzed electrophoretically in a 1.5% agarose gel with ethidium bromide staining. An image was obtained, and the bands were quantified with an image quantifier (440CF; Kodak, New Haven, CT, U.S.A.)

Microscopic assessment of nuclear chromatin condensation and fragmentation

Cells grown on glass-bottom (35 mm) dishes (MatTek Corp., Ashland, MA, U.S.A.) were stained with a fluorescent dye, Hoechst 33342 (Molecular Probes). At 0, 0.25, 0.5, 1, 3, and 5 h after 1 day of hypoxia, the cells were fixed for 30 min in a solution containing 4% formaldehyde in phosphate-buffered saline (PBS), and then incubated in PBS with 1 μg/ml of the dye for 30 min. The cells were washed twice

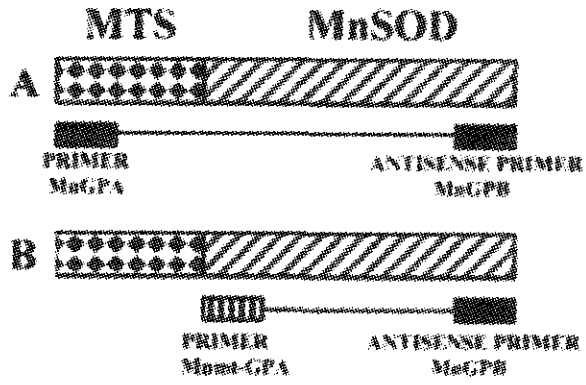

FIG. 1. Schematic diagram of MnSOD gene and primer setting. **(A)** Construct and primer range for MnSOD and primers used to generate and detect full-length MnSOD cDNA and mRNA. **(B)** Construct of the full-length MnSOD and primers used to generate and detect MTS-lacking MnSOD cDNA and mRNA.

with PBS and then twice with water. Fluorescence was visualized using an IX90 inverted microscope with a UPlanAPO 20× objective lens (Olympus Optical Co.). The dye was excited at 340 nm, and the emission was filtered with a 510-nm barrier filter. Photographs of microscope fields were taken using a C5810–01 color chilled 3CCD camera (Hamamatsu Photonics K.K.). More than 500 cells per culture dish were counted, and counts were made in three separate cultures per each H/R treatment. Analyses were performed without any knowledge of the H/R treatment history of the culture dishes. The percentage of apoptotic cells (apoptotic index) in each culture dish was determined.

Bioimaging of nitric oxide (NO)

Diaminofluoresceins (DAFs) (Daiichi Pure Chemicals, Tokyo, Japan) are fluorescent indicators for NO (17). They do not react with NO itself, but with NO+ equivalents, such as nitric trioxide (N_2O_3), which are produced by autoxidation of NO. Diaminofluorescein-FM diacetate (DAF-FM DA), which was a kind gift from Daiichi Pure Chemicals, is a newly synthesized DAF, which permeates well into cells and is quickly converted into water-soluble DAF-FM by esterases in the cytosol, where the dye can remain for a long time. Under aerobic conditions, DAF-FM traps NO to yield highly fluorescent triazofluoresceins (DAF-FM Ts) by nitrosation and dehydration. DAF-FM Ts are not formed in the presence of NO. Glass-bottom (35 mm) dishes (MatTek Corp.) with monolayers were prepared for staining with DAF-FM DA. At 0, 1, 2, 3, and 6 h after a H/R treatment, the cell culture medium was replaced with a modified Hanks' balanced salt solution containing 10.0 m*M* HEPES, 1.0 m*M* $MgCl_2$, 2 m*M* $CaCl_2$, and 2.7 m*M* glucose adjusted to pH 7.3 ± 0.05. The cells were then loaded with 10 μ*M* DAF-FM DA by incubation for 30 min at 37°C. Bioimages of DAF-FM DA were acquired using a CSU-10 confocal laser scanning unit (Yokogawa Electric Co.) coupled to an IX90 inverted microscope with UPlanAPO X20 objective lens (Olympus Optical Co.) and C5810–01 color chilled 3CCD camera (Hamamatsu Photonics. K.K.). The DAF-FM DA was excited at 488 nm, and the emission was filtered using a 515-nm barrier filter. The intensity of the laser beam, the exposure time of the 3CCD camera, and the gain of the amplifier were held at 500 μW, 1.0 s, and 18 db, respectively, to allow quantitative comparisons of the relative fluorescent intensity of the cells between groups. Cells were chosen and scanned at more than three spots for analysis on a random basis. The values for the average fluorescence intensity per cell were obtained using IPLab Spectrum version 3.0 (Scanalystics Inc., Fairfax, VA, U.S.A.) software with some modification of the program by the author (H.J.M). The fluorescent intensity (which was acquired by confocal laser microscopy and analyzed by computer) following H/R treatment divided by the intensity of no-treatment intact cells was calculated as the relative fluorescent intensity, which indicates the "increment" of the intensity induced by H/R treatment in each cell. Note that the relative fluorescent intensity is *not* the ratio of the fluorescent intensity to the control plasmid transfected cells or parental cells.

Relative levels of mitochondrial ROS

Dihydrorhodamine 123 (dhRho) (Molecular Probes) is an oxidation-sensitive lipophilic dye that enters a cell and fluoresces when oxidized by mitochondrial ROS to the positively charged rhodamine 123 derivatives. The relative level of mitochondrial ROS loaded with dhRho was quantified by a confocal laser microscope image using the same procedures described for DAF measurements, except that the final concentration of the dye used in the study was 10 μg/ml.

Immunofluorescent staining for 4-hydroxy-2-nonenal (HNE)

Glass-bottom (35 mm) dishes (MatTek Corp.) with monolayers were prepared for immunofluorescent staining with a monoclonal antibody directed against proteins modified by the major membrane lipid peroxidation product, HNE. This monoclonal antibody (NOF Corp., Tokyo, Japan), specific for HNE-modified proteins, was raised by immunizing mice with an HNE-modified keyhole limpet hemocyanin conjugate (40). The antibody was tested for cross-reactivity toward glutaraldehyde, formaldehyde, 1-hexanal, 2-hexanal, 4-hydroxy-2-hexanal, and 2-nonenal. Enzyme-linked immunosorbent assays with these potential competitors were performed. The results indicated that the anti-HNE antibody is highly specific to HNE-derived modifications to protein. At 0, 1, 2, 3, and 6 h after the H/R treatment, cells were fixed with 4% formaldehyde/PBS at room temperature for 30 min and then rinsed twice with PBS, and membranes were permeabilized by incubation in 95% ethanol with 5% acetic acid for 10 min. After washing with PBS twice, the cells were incubated for 4 min in a blocking solution(1% bovine serum albumin in PBS) and for 1 h in anti-HNE mouse monoclonal antibody at a dilution factor of 1:200. The cells were rinsed twice with 0.1% bovine serum albumin in PBS and reincubated with Alexa Fluor 488 goat anti-mouse IgG (H+L) conjugate (Molecular Probes) for 1 h at room temperature. Image acquisition and analysis were similar to that of DAF-FM DA, except that the exposure time of the 3CCD camera was 10 s.

Statistical analysis

A statistical analysis was performed by an analysis of variance, followed by Fisher's post hoc tests. A p value of <0.05 was considered to be statistically significant. Data were presented as the means ± SE. Calculations were performed with a statistical package, StatView 5.0J (SAS Institute Inc., Cary, NC, U.S.A.), on a Power Macintosh G3 (Apple Computer, Inc.).

RESULTS

Isolation of KP4 transfectants expressing MnSOD and mito(−) MnSOD

The production of active MnSOD in these transfectants was investigated in cell lysates. The parent KP4 cells, two vector clone transfectants (vec-1 and -2) (from six clones), two mito(−) MnSOD clones [mito(−)-4 and -6] (from six clones), and three MnSOD clones (MnSOD-5, -9 and -10) (from 12 clones) were examined for MnSOD activity. The intensity of MnSOD was semiquantified from the captured image. MnSOD activity of the parental cells was normalized to 1, and the relative MnSOD activities of the other cells were calculated (Table 1). The increase in MnSOD activity in the clones MnSOD-5, -9, and -10 was clearly detectable, *i.e.*, the MnSOD activity in the MnSOD-transfected cells was greater than that in the control cells. The relative activities of MTS-lacking MnSOD [mito(−)] transfectants were also greater compared with that in the control cells, although they were generally slightly less than those in the MnSOD clones.

RT-PCR detection of mRNA in MnSOD cells and mito(−) cells

To ascertain the expression of MnSOD and MnSOD lacking MTS, total cellular RNA was first reverse-transcribed into cDNA with an antisense primer, MnGPB, and then subsequently amplified by PCR. To examine the full-range MnSOD including MTS gene expressions, a sense primer (MnGPA) and an antisense primer (MnGPB) were used for PCR amplification, whereas to examine the MnSOD without MTS gene expression, a sense primer (Mnmt-GPA) and an antisense primer (MnGPB) were used for PCR amplification (Fig. 1). Increased MnSOD mRNA levels were confirmed in MnSOD-5, -9, and -10 using the MnGPA primer (Fig. 2A). However,

TABLE 1. RELATIVE INTENSITY OF MNSOD ACTIVITY

Cell line	*Relative intensity*
KP4	1
Vec-1	1.091 ± 0.040
Vec-2	1.207 ± 0.292
Mito(−)-4	2.320 ± 0.494
Mito(−)-6	1.861 ± 0.191
MnSOD-5	2.471 ± 0.362
MnSOD-9	3.024 ± 0.482
MnSOD-10	2.570 ± 0.505

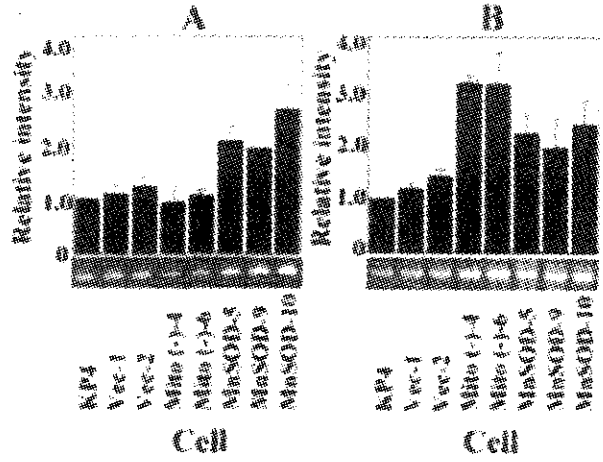

FIG. 2. RT-PCR detecting mRNA of the full length of normal MnSOD, or MTS-lacking MnSOD. (A) The full-length MnSOD including MTS gene expression, a sense primer (MnGPA), and an antisense primer (MnGPB) were used for PCR amplification. The full-length mRNA levels were higher in MnSOD-5, -9, -10 compared with that in the controls and mito(−) clones. **(B)** MnSOD without MTS, a sense primer (Mnmt-GPA), and an antisense primer (MnGPB) were used for the PCR amplification. The transfected mRNA was higher in MnSOD-5, -9, -10, mito(−) -4 and -6 transfectants, compared with the untransfected and vector alone controls.

when the Mnmt-GPA primer was used, not only did the mRNA for MnSOD-5, -9, and -10 increase, but higher mRNA levels of the MnSOD products for mito(−)-4 and -6 transfectants were observed (Fig. 2B). These results are consistent with those found for MnSOD activity and demonstrate that the transfection of MnSOD lacking MTS vectors was successful in mito(−) -4 and -6 transfectants.

Effect of MnSOD on H/R-induced apoptotic cell death

To determine the effect of H/R treatment on apoptotic cell death, we performed a microscopic assessment of nuclear chromatin condensation and fragmentation assay using Hoechst 33342 staining. For control experiments, we examined the change in the apoptotic index (number of apoptotic cells/500 cells counted) in air (Fig. 3A) or hypoxic conditions alone (Fig. 3B). As shown in Fig. 3, in cells grown up to 5 days in either air or hypoxic conditions, no increase in the apoptotic index was observed. In H/R experiments (Fig. 4), the apoptotic index was determined in cells cultured in air for 0, 0.25, 0.5, 1, 3, and 5 days after the 1-day hypoxia treatment. Except for MnSOD-5, -9, and -10, the apoptotic index significantly increased at 1 day, and by 5 days declined to the control levels in all cells. The absolute number of apoptotic cells and the relative index, which was calculated as the ratio of apoptotic cell count on day 1 to that on day 0, are listed in Table 2. The results show that the relative apoptotic index was suppressed in the full-length MnSOD transfected cells compared with that of the KP4, vec-1 and -2, and mito(−) transfectants. This result indicates that only when MnSOD is

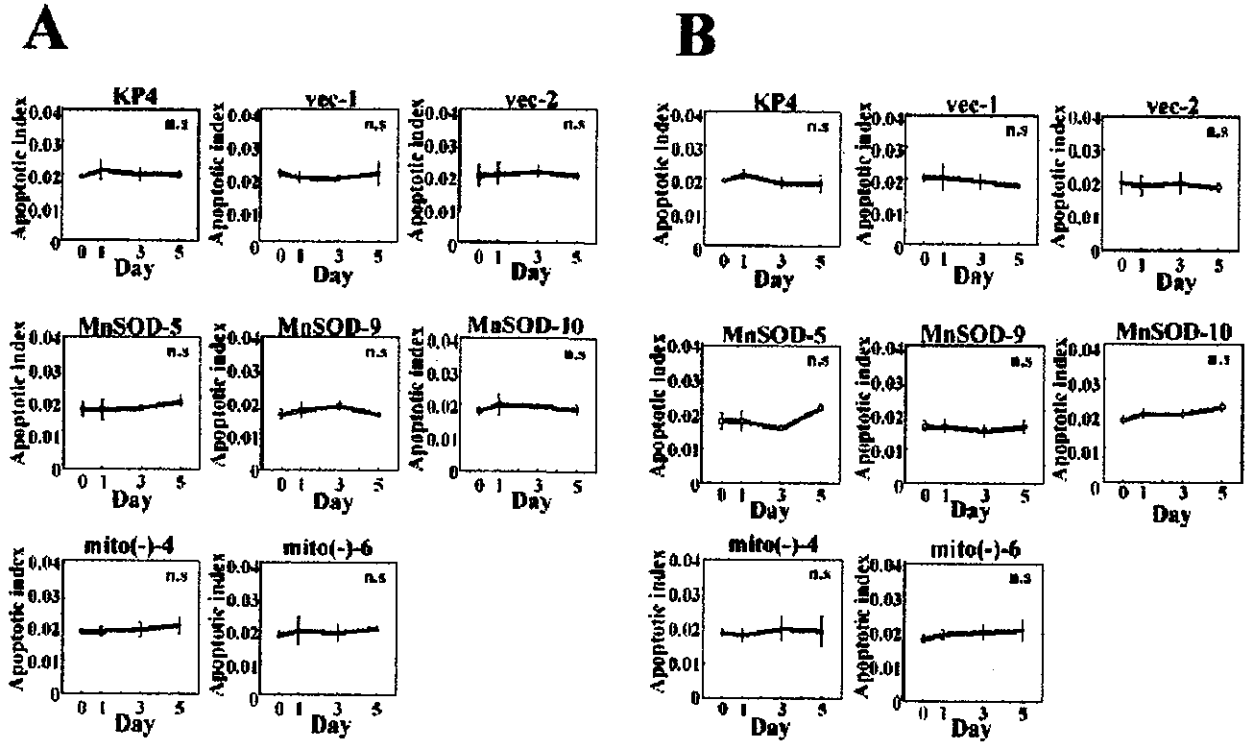

FIG. 3. No change in the apoptotic index as a function of time in air or hypoxic conditions. The change in apoptotic index (number of apoptotic cells/500 cells counted) in air **(A)** or hypoxia alone **(B)** is presented. n.s, not significant.

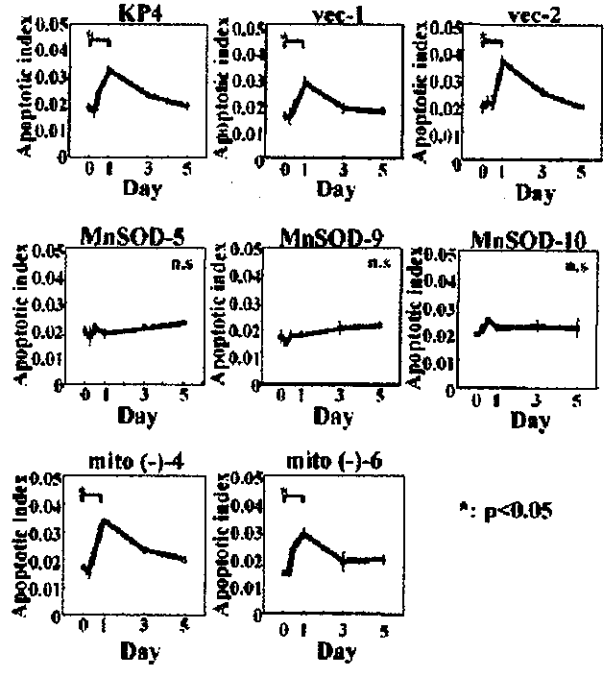

FIG. 4. Apoptotic index for H/R condition. The apoptotic index in each cell line at 0, 0.25, 0.5, 1, 3, and 5 days in air after 1 day of hypoxia treatment (H/R treatment) was determined. With the exception of MnSOD-5, -9, and -10, the apoptotic index increased to a maximum in 1 day, followed by a decline in all cells. The full-length MnSOD, and not MTS-lacking MnSOD, suppresses H/R treatment-induced apoptosis. n.s, not significant; $*p < 0.05$.

localized in the mitochondria can it suppress H/R-induced apoptosis.

MnSOD does not influence hypoxia-induced NO generation

To determine the effect of MnSOD on H/R treatment-induced intracellular NO generation, a dye sensitive to a change in the intracellular NO, DAF-FM DA, was used. To ascertain NO generation ability in every cell type, we irradiated cells with 15 Gy and examined NO generation at 2 h fol-

TABLE 2. NUMBER OF APOPTOTIC CELLS AND THE RELATIVE APOPTOTIC INDEX

Cell line	*Apoptotic cell day 1/day 0**	*Relative apoptotic index*
KP4	16.33 ± 0.88 / 9.33 ± 0.67	1.75 ± 0.09
Vec-1	14.00 ± 1.00 / 7.67 ± 0.67	1.83 ± 0.13
Vec-2	18.00 ± 1.00 / 9.67 ± 1.20	1.86 ± 0.10
Mito(−)-4	17.00 ± 0.00 / 8.67 ± 0.33	1.96 ± 0.00
Mito(−)-6	14.33 ± 0.88 / 7.33 ± 0.33	1.95 ± 0.12
MnSOD-5	9.33 ± 0.88 / 9.67 ± 0.88	0.97 ± 0.09†
MnSOD-9	9.00 ± 0.58 / 8.67 ± 1.20	1.04 ± 0.07†
MnSOD-10	11.00 ± 0.58 / 9.67 ± 0.33	1.14 ± 0.06†

*Absolute apoptotic cell number per 500 cells. Data shown in the table are the averages of three independent experiments.
†$p < 0.05$ versus KP4, $p < 0.05$ versus vec-1, $p < 0.05$ versus vec-2, $p < 0.05$ versus mito(−)-4, and $p < 0.05$ versus mito(−)-6.

lowing the irradiation. The results show 12–20% increases in NO generation in all cell types, indicating that every cell line has the ability to generate NO against oxidative stress (data not shown). In the next H/R experiments, the dye was loaded at 0, 1, 2, 3, and 6 h in air after 1 day of hypoxia treatment, and the images were acquired after 30 min of incubation. The fluorescent intensity was not changed after the H/R treatment in all cell types (Fig. 5). This result indicates that NO was not a major contributor of H/R-induced cell injury.

MnSOD suppresses H/R-induced mitochondrial ROS generation

To determine the effect of MnSOD on H/R-induced mitochondrial ROS generation, a dye sensitive to a change in mitochondrial ROS was used. For an analysis of the levels of mitochondrial ROS, we utilized the same analytic technique used for NO detection. The dye was loaded at 0, 1, 2, 3, and 6 h in air after 1 day of hypoxia treatment, and the images were acquired after 30 min of incubation. The change in the relative fluorescent intensity is shown in Fig. 6. This result shows that the relative fluorescent intensity of the dhRho was reduced in the MnSOD-transfected cells compared with the KP4, vec-1, and -2 cells, indicating that MnSOD suppresses H/R treatment-induced ROS generation in mitochondria. In addition, the change in ROS in the mito(−) cells following the H/R treatment was similar to that of the control and vector cells, indicating MnSOD lacking MTS had no effect on H/R-induced mitochondrial ROS levels.

H/R induces lipid peroxidation

To determine if changes of mitochondrial ROS generation are accompanied by an increase in lipid peroxidation products, the levels of HNE-modified proteins were evaluated by immunohistochemical staining. Preliminary experiments showed that there was no significant change in HNE-modified protein-staining intensity among all cell types using the intact cells (data not shown). The change in the relative HNE-modified protein-staining intensity in each cell line, which was obtained at 0, 1, 2, 3, and 6 h in air after 1 day of hypoxia treatment, is shown in Fig. 7. The result shows that the relative HNE-modified protein-staining intensity was suppressed in the MnSOD-transfected cells, but not in vector alone or MnSOD lacking MTS transfected cells. These results indicate that normal MnSOD, and not MnSOD lacking MTS, suppresses the levels of the H/R treatment-induced formation of intracellular HNE-modified proteins.

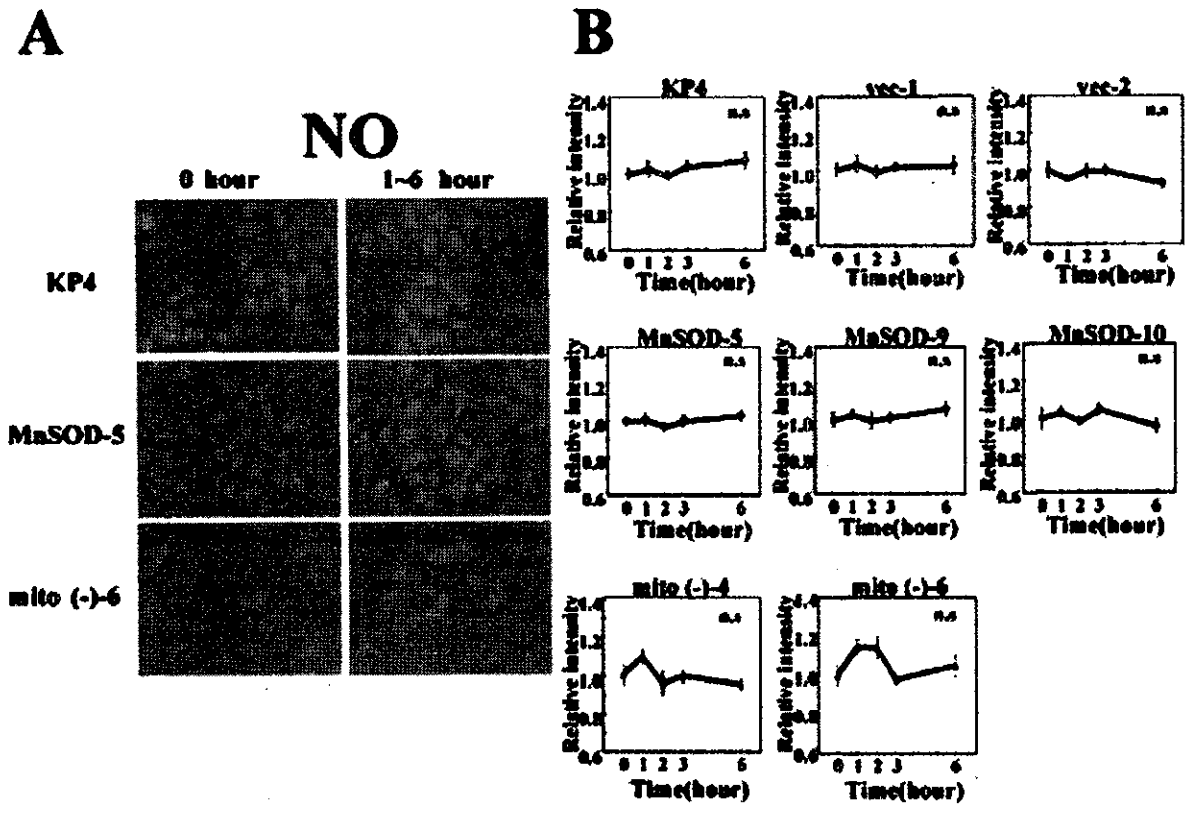

FIG. 5. Intracellular NO generation. The intracellular NO generation in each cell line at 0, 1, 2, 3, and 6 h in air after 1 day of hypoxia treatment (H/R treatment) was determined. No increase in the intracelluar NO levels was observed in all cell lines examined. The apparent increase in NO level did not achieve statical significance. **(A)** Representative photographs of cell stained with DAF. **(B)** Relative fluorescent intensity of DAF versus time (hours) in air following 1 day of hypoxia treatment (H/R treatment). n.s, not significant.

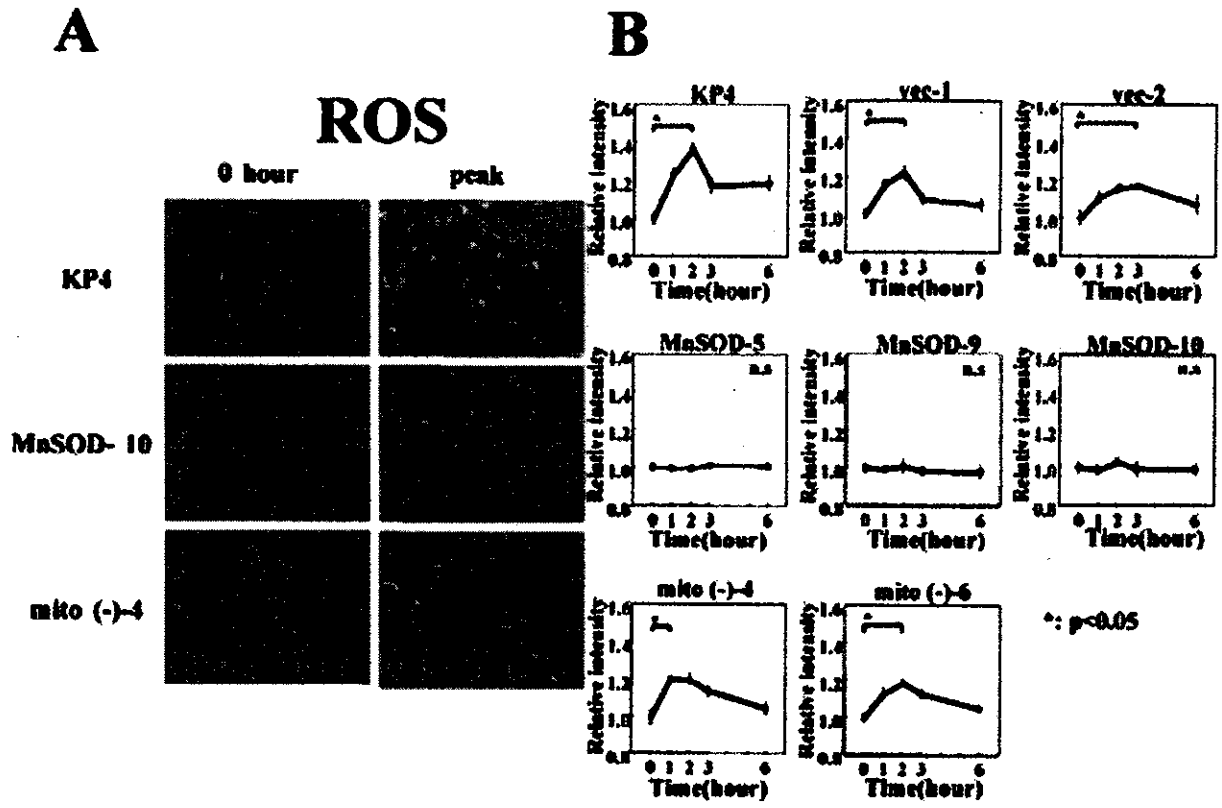

FIG. 6. Mitochondrial ROS generation. The levels of ROS in mitochondria in each cell line at 0, 1, 2, 3, and 6 h in air after 1 day of hypoxia treatment (H/R treatment) were determined. The relative fluorescent intensity of the dhRho was reduced in the MnSOD transfected cells compared with the KP4, vec-1 and -2, and mito(−) cells. **(A)** Representative images of cells examined for dhRho, at 0 h or at the peak times. **(B)** Relative fluorescent intensity of dhRho versus time (hours) in air following 1 day of hypoxia treatment (H/R treatment). n.s, not significant; $*p < 0.05$.

Correlation between mitochondrial ROS, intracellular lipid peroxidation products, and cell death

To understand better the relationship between mitochondrial ROS, intracellular lipid peroxidation, and cell death, we used a scattergram to plot (a) the relative apoptotic index against the relative dhRho (ROS) staining intensity, (b) the relative apoptotic index against the relative HNE-modified protein-staining intensity, and (c) the relative HNE-modified protein-staining intensity against the relative ROS staining intensity, and then analyzed the data using linear regression analysis. Figure 8A shows a linear-regression analysis of the relative apoptotic index against the relative mitochondrial ROS staining intensity ($r = 0.818$, $p = 0.018$). Figure 8B shows a linear-regression analysis of the relative apoptotic index versus the relative HNE-modified protein-staining intensity ($r = 0.933$, $p = 0.018$). These results show a strong positive correlation between the mitochondrial ROS, the intracellular lipid peroxidation products, and apoptosis. Figure 8C illustrates a linear-regression analysis of the relative ROS staining intensity versus the HNE-modified protein-staining intensity ($r = -0.856$, $p = 0.020$), indicating a correlation between the relative ROS staining intensity and that of HNE-modified protein adducts. Thus, intracellular mitochondrial ROS staining intensity and relative HNE-modified protein-staining intensity have a strong correlation with apoptosis, and there is a strong correlation with mitochondrial ROS staining intensity and HNE-modified protein-staining intensity.

Localization of MnSOD, MnSOD lacking MTS, and MTS signal only in KP4 cells

To examine localization of MnSOD, MnSOD lacking MTS [MnSOD mito(−)], and MTS signal alone (Mito signal), the cDNA was linked with the pEGFP vector and then transfected with KP4 cells. To localize mitochondria, the same cells were stained with MitoTracker Red CMXRos. A merged double image of GFP and MitoTracker was made to verify coexistence of MnSOD, MnSOD lacking MTS, or MTS alone in mitochondria. Figure 9 shows that MnSOD was localized in mitochondria, as shown by the color yellow (green plus red) in the double image of pEGFP and Mitotracker. A similar image was taken for MTS alone (Mito signal) in the double image, where a yellow color is clearly shown. However, for MTS-lacking MnSOD [MnSOD mito(−)], only a few yellow color regions can be seen in the double color picture, indicating the most of the MnSOD lacking MTS was localized in cytosol, although the fluorescent intensity of pEGFP in the image is unclear or obscure in the cytosol.

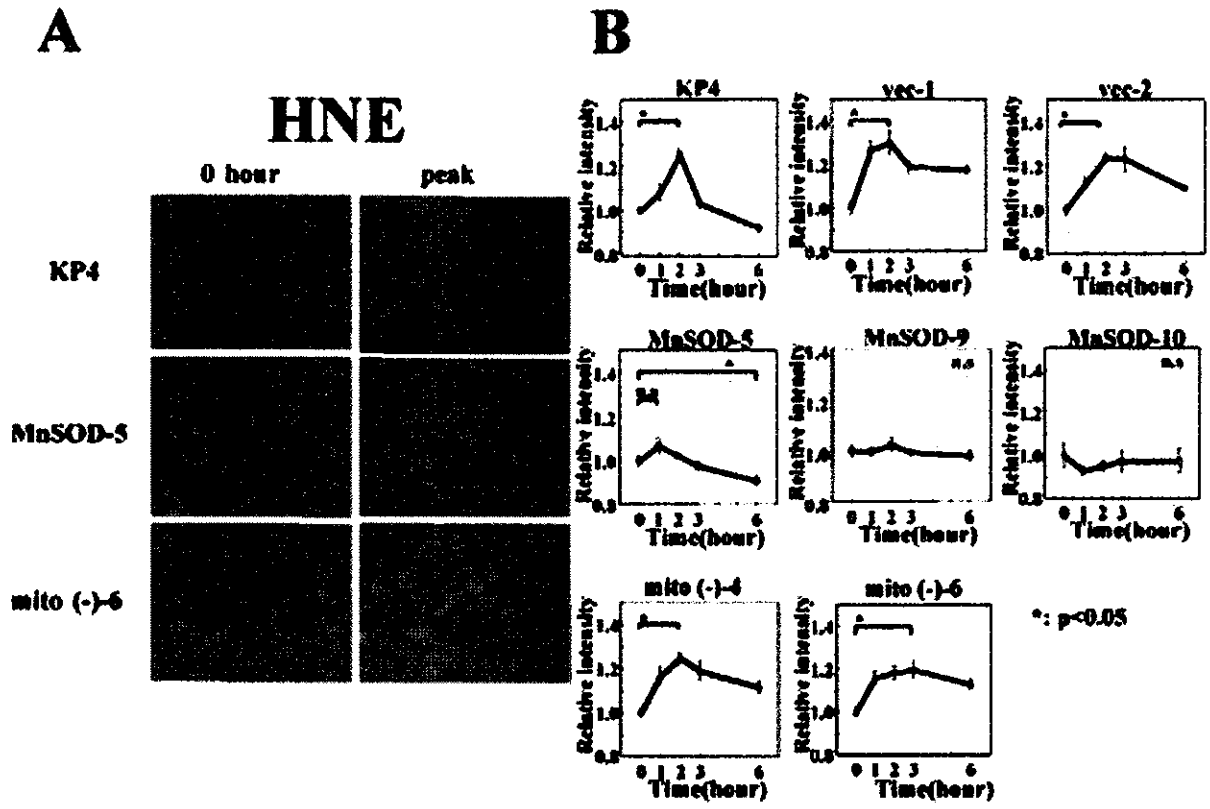

FIG. 7. Intracellular HNE adducts. The intracellular levels of HNE protein adducts in each cell line at 0, 1, 2, 3, and 6 h in air after 1 day of hypoxia treatment (H/R treatment) were determined. **(A)** Representative photographs of cell staining with an antibody against HNE protein adducts at 0 h or peak hours. **(B)** Relative fluorescent intensity of HNE protein adducts versus time (hours) in air following 1 day of hypoxia treatment (H/R treatment). n.s, not significant; $*p < 0.05$.

DISCUSSION

Using a human pancreatic tumor cell line, KP4, we first examined the effects of H/R on ROS production, lipid peroxidation, and cellular viability following 1 day of hypoxia and subsequent exposure to air. The results show that H/R increased ROS, lipid peroxidation, and apoptosis, although the apoptosis frequency was small. In this study, we investigated whether an enhanced expression of mitochondrial MnSOD, a superoxide-scavenging enzyme, can protect cells against H/R.

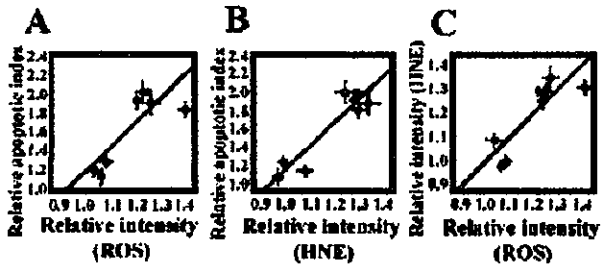

FIG. 8. Correlation between mitochondrial ROS, intracellular lipid peroxidation protein adducts, and cell death. (A) Linear-regression analysis showing the relationship between the relative apoptosis index and the relative dhRho staining intensity (mitochondrial ROS) after H/R treatment ($r = 0.818, p = 0.018$). **(B)** Relationship between the relative apoptosis index and the relative HNE protein-adducts staining intensity (intracellular lipid peroxidation products) ($r = 0.933, p = 0.018$). **(C)** Relationship between the relative dhRho staining intensity and the relative HNE protein adducts staining ($r = -0.856, p = 0.020$). Mitochondrial ROS, intracellular lipid peroxidation products, and apoptosis have a strong correlation with each other.

We found that H/R-produced apoptosis is suppressed by MnSOD, but not by mito(−) MnSOD, which is not located in the mitochondria. These results signify the importance of mitochondrial localization of MnSOD. It has been shown that adenoviral gene transfer with MnSOD is effective in reducing the extent of *in vivo* I/R injury in the rat heart (1) and in mouse liver (50), but expression of copper/zinc SOD (Cu/ZnSOD) did not function in protection in the mouse liver model (50). Given the fact that the MnSOD and Cu/ZnSOD used in these studies were mainly expressed in the mitochondria and cytosol, respectively, these results are consistent with our results. Our results further indicate that not only is active MnSOD important, but also it must be located in the mitochondria for the observed protection.

The reaction between superoxide radicals and NO to form peroxynitrite is a subject under considerable study. Superoxide radicals can react at diffusion rates with NO to form peroxynitrite, a potent biological oxidant. In this study, however, we could not find evidence of further NO induction by hypoxia treatment. This is not surprising, because oxygen is an essential substrate for NO synthesis. Our results are also consistent with various other reports that indicate that hypoxia

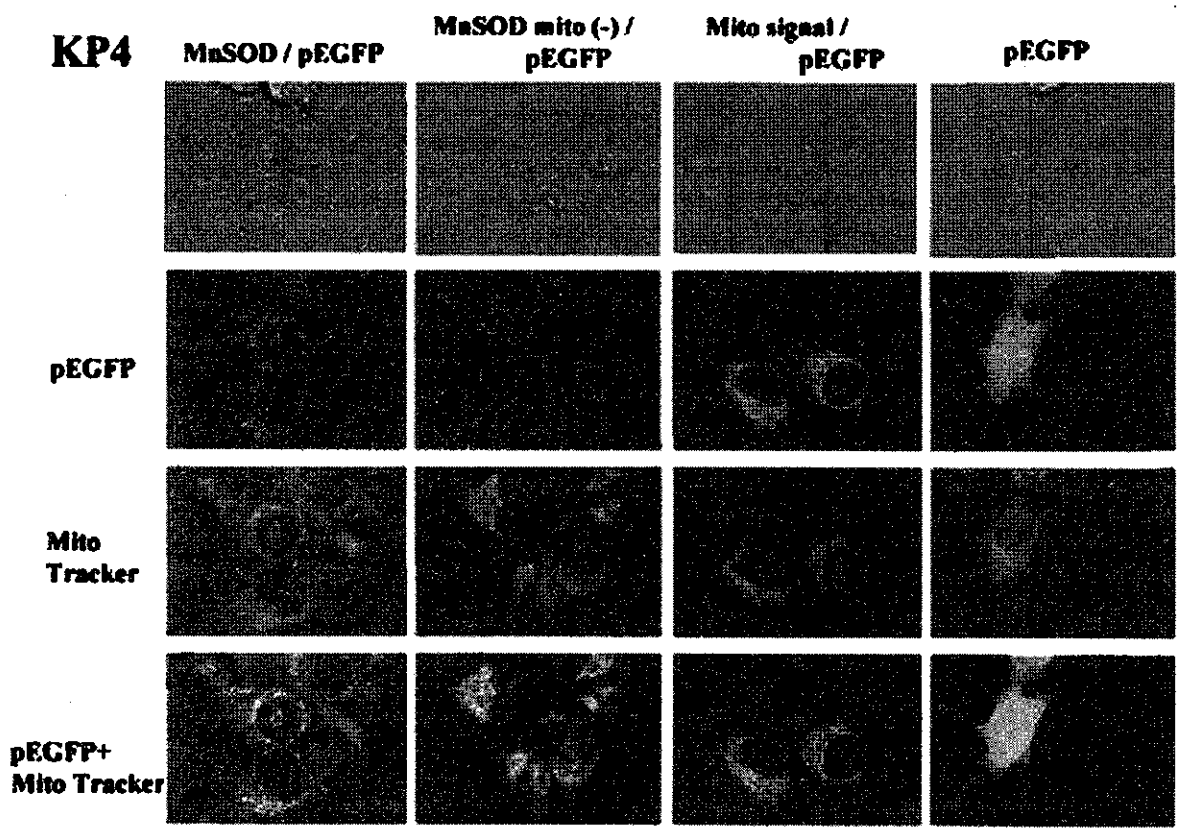

FIG. 9. Localization of MnSOD, MnSOD lacking MTS, and MTS alone in KP4 cells. Localization of full-length MnSOD, MnSOD lacking MTS [MnSOD mito (−)], and MTS signal alone (Mito signal) is shown. GFP was visualized using the pEGFP transfection sytem. To locate mitochondria, the same cells were stained with MitoTracker Red CMXRos. Merged double images of GFP and MitoTracker were made to identify MnSOD in mitochondria. MnSOD was localized in mitochondria, as shown by the yellow color (green plus red) in the double image of pEGFP and MitoTracker. A similar image was taken for MTS alone (Mito signal) in the double image, where a yellow color is clearly shown. However, for MTS lacking MnSOD [MnSOD mito (−)], only a few yellow color regions can be seen in the double color picture, indicating that most of the MnSOD lacking MTS was localized in cytosol, although the fluorescent intensity of pEGFP is unclear or obscure in cytosol in the picture.

limits NO synthesis even when NO synthase is overexpressed (for review, see 19). As ROS are increased without a concurrent increase in NO production in the H/R model, it is likely that the observed increase in HNE-modified proteins is mediated via hydroxyl radical generation. The finding that increased expression of MnSOD abolished the increased levels of HNE-modified proteins under H/R further supports this possibility.

Our results indicating that only MnSOD and not mito(−) transfectants suppress the formation of HNE-modified proteins suggest that superoxide production in the mitochondria is important for the production of HNE-modified proteins under conditions of H/R. Our results further indicate that the localization of active MnSOD in the mitochondrion is important for the suppression of ROS production and subsequent formation of HNE protein adducts. These results suggest that H/R-induced apoptosis is linked to the production of ROS and its toxic products.

Mitochondrial damage and the role of mitochondria in apoptosis are well established in various pathological conditions. However, it is largely unknown whether mitochondria are the sources or targets in such apoptosis events. Our results suggest that induction of oxidative injury in mitochondria is an upstream event leading to apoptosis in H/R-induced cell death.

Endogenous MnSOD is a nuclear-encoded protein that is cotranslationally transported into mitochondria where the signal peptide is removed and Mn is inserted to produce active proteins. The role of MnSOD in protecting against oxidative stress-mediated cell death has been demonstrated in organisms ranging from bacteria to mammals. In all studies reported thus far, it has been assumed that the effect of MnSOD is due to its location in mitochondria. However, the question remains to be investigated as to whether enzyme localized outside mitochondria has any protective effect. Our results reported here clearly demonstrate that expression of active MnSOD outside mitochondria was not effective. Although it is unclear how MnSOD located outside mitochondria acquires its Mn and proper conformation for its activity, our results from activity assay, mRNA RT-PCR assay, apoptosis observation, and colocalization studies (Table 1, Figs. 2, 4, and 9) provide strong support that active MnSOD outside mitochondria is not effective in protecting against H/R-induced apoptosis. Our GFP vector images (Fig. 9) show that

only small amounts of transfectants of MnSOD mito(−) are found in mitochondria. The distribution of GFP outside mitochondria of the MnSOD and Mito signal alone may indicate that the intensity of MnSOD lacking MTS was low because of a wide dispersion over cytosol. Although our finding that the MnSOD construct lacking MTS expresses active MnSOD protein outside mitochondria is unexpected; this phenomenon has been observed for other antioxidant enzymes as well. For example, Tamura *et al.*(37) demonstrated a much greater enhancement of cellular resistance to oxidant challenge by CHO cells by stable transfection with leader sequence of glutathione reductase (GR) cDNA than they observed in a construct lacking the MTS, which produced comparable increases in the total cellular GR activities, but did not increase mitochondrial GR activities (29, 37, 38). Arai *et al.* (2) demonstrated the effect of phospholipid hydroperoxide glutathione peroxidase, which is naturally synthesized as a long form (the L-form; 23 kDa) and a short form (the S-form; 20 kDa). The long form contains a mitochondrial targeting leader sequence, whereas the short form lacks the leader sequence. Cells transfected with the L-form containing vector were more resistant against oxidative stress, including potassium cyanide, rotenone (chemical hypoxia), and exogenous *tert*-butyl hydroperoxide oxidant injuries, compared with those cells transfected with the S-form containing vector (2). Wong (46) demonstrated that MnSOD without the mitochondrial leading targeting signal failed to protect against radiation, whereas the reduction of normal cytosolic Cu/ZnSOD or normally extracellularly expressed SOD to mitochondria with MTS resulted in protection against radiation. These results suggest that MnSOD, which is located in cytosol, does not function to prevent against H/R treatment-induced oxidative damage and cell death, and only when the enzyme is located in mitochondria does MnSOD have a function. Taken together, these data support the critical role of mitochondria localization of antioxidant enzymes for the protection against cellular injury from outside stress initiated in the mitochondrion.

In summary, the findings shown in study indicated that (a) H/R induced increased mitochondrial ROS production, lipid peroxidation protein-adducts, and subsequent apoptosis; (b) these processes were suppressed by active MnSOD in the mitochondria but not in the cytosol even when the MnSOD is active; and (c) the results support the overall hypothesis depicted in Fig. 10 showing that H/R triggers mitochondrial ROS production and generation of lipid peroxidation products, and subsequently accelerates cell death and its inhibition by MnSOD.

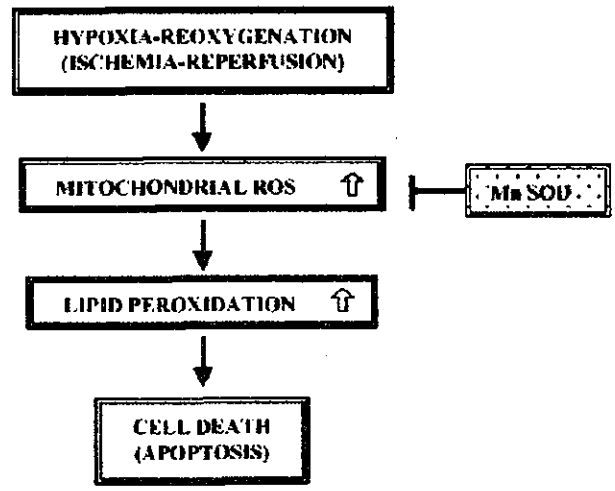

FIG. 10. Schematic diagram of a hypothesis on how ROS generation and lipid peroxidation products affect cell death (apoptosis) and its prevention by MnSOD after H/R treatment.

ACKNOWLEDGMENTS

The authors wish to thank Dr. Makoto Akashi (NIRS) for MnSOD cDNA, and Ms Chizuru Yamaguchi and Dr. Yoichiro Iwashita for technical assistance. This study was partially supported by "Ground Research Announcement for Space Utilization" promoted by Japan Space Forum, and The Nuclear Cross-Over Research Study, Grant-in Aid for Scientific Research (C) (2) #10671786, #12671844, #14207078, and #15659451 of Ministry of Education, Culture, Sports, Science and Technology, Japan.

ABBREVIATIONS

Cu/ZnSOD, copper/zinc superoxide dismutase; DAF, diaminofluorescein; DAF-FM DA, diaminofluorescein-FM diacetate; dhRho, dihydrorhodamine 123; DMEM, Dulbecco's modified Eagle medium; GFP, green fluorescent protein; GR, glutathione reductase; HNE, 4-hydroxy-2-nonenal; H/R, hypoxia followed by reoxygenation; I/R, ischemia/reperfusion; mito(−), lacking MTS; mito(−)-, MTS lacking MnSOD transfected cell clone; MnSOD, manganese superoxide dismutase (EC 1.15.1.1); MnSOD-, MnSOD transfected cell clone; MTS, mitochondrial targeting signal; NO, nitric oxide; PBS, phosphate-buffered saline; ROS, reactive oxygen species; SOD, superoxide dismutase; vec-, vector alone transfected cell clone.

REFERENCES

1. Abunasra HJ, Smolenski RT, Morrison K, Yap J, Sheppard MN, O'Brien T, Suzuki K, Jayakumar J, and Yacoub MH. Efficacy of adenoviral gene transfer with manganese superoxide dismutase and endothelial nitric oxide synthase in reducing ischemia and reperfusion injury. *Eur J Cardiothorac Surg* 20: 153–158, 2001.
2. Arai M, Imai H, Koumura T, Yoshida M, Emoto K, Umeda M, Chiba N and Nakagawa Y. Mitochondrial phospholipid hydroperoxide glutathione peroxidase plays a major role in preventing oxidative injury to cells. *J Biol Chem* 274: 4924–4933, 1999.
3. Beauchamp C and Fridovich I. Superoxide dismutase: improved assays and an assay applicable to acrylamide gels. *Anal Biochem* 44: 276–287, 1971.
4. Bienvenu P, Caron L, Gasparutto D, and Kergonou JF. Assessing and counteracting the prooxidant effects of anticancer drugs. *EXS* 62: 257–265, 1992.

5. Boveris A and Cadenas E. Mitochondrial production of superoxide anions and its relationship to the antimycin insensitive respiration. *FEBS Lett* 1: 311–314, 1975.
6. Brown JM. Evidence for acutely hypoxic cells in mouse tumours, and a possible mechanism of reoxygenation. *Br J Radiol* 52: 650–656, 1979.
7. Brown JM. The hypoxic cell: a target for selective cancer therapy—eighteenth Bruce F. Cain Memorial Award lecture. *Cancer Res* 59: 5863–5870, 1999.
8. Carlioz A and Touati D. Isolation of superoxide dismutase mutants in *Escherichia coli:* is superoxide dismutase necessary for aerobic life? *EMBO J* 5: 623–630, 1986.
9. Chomczynski P and Sacchi N. Single-step method of RNA isolation by acid guanidinium thiocyanate–phenol–chloroform extraction. *Anal Biochem* 162: 156–159, 1987.
10. Engelhardt JF. Redox-mediated gene therapies for environmental injury: approaches and concepts. *Antioxid Redox Signal* 1: 5–27, 1999.
11. Farr SB, D'Ari R, and Touati D. Oxygen-dependent mutagenesis in *Escherichia coli* lacking superoxide dismutase. *Proc Natl Acad Sci USA* 83: 8268–8272, 1986.
12. Halliwell B and Gutteridge JMC. Free radicals, other reactive species and disease. In: *Free Radicals in Biology and Medicine,* 3rd edit., edited by Halliwell B and Gutteridge JMC. Oxford, U.K.: Oxford University Press, 1999, pp.617–783.
13. Hirose K, Longo DL, Oppenheim JJ, and Matsushima K. Overexpression of mitochondrial manganese superoxide dismutase promotes the survival of tumor cells exposed to interleukin-1, tumor necrosis factor, selected anticancer drugs, and ionizing radiation. *FASEB J* 7: 361–368, 1993.
14. Ho YS and Crapo JD Isolation and characterization of complementary DNAs encoding human manganese-containing superoxide dismutase. *FEBS Lett* 229: 256–260, 1988.
15. Kiningham KK, Oberley TD, Lin S, Mattingly CA, and St Clair DK. Overexpression of manganese superoxide dismutase protects against mitochondrial-initiated poly(ADP-ribose) polymerase-mediated cell death. *FASEB J* 13: 1601–1610, 1999.
16. Knisely JP and Rockwell S. Importance of hypoxia in the biology and treatment of brain tumors. *Neuroimaging Clin N Am* 12: 526–536, 2002.
17. Kojima H, Nakatsubo N, Kikuchi K, Kawahara S, Kirino Y, Nagoshi H, Hirata Y, and Nagano T. Detection and imaging of nitric oxide with novel fluorescent indicators: diaminofluoresceins. *Anal Chem* 70: 2446–2453, 1998.
18. Lebovitz RM, Zhang H, Vogel H, Cartwright J Jr, Dionne L, Lu N, Huang S, and Matzuk MM. Neurodegeneration, myocardial injury, and perinatal death in mitochondrial superoxide dismutase deficient mice. *Proc Natl Acad Sci U S A* 93: 9782–9787, 1996.
19. Le Cras TD and McMurtry IF. Nitric oxide production in the hypoxic lung. *Am J Physiol Lung Cell Mol Physiol* 280: L575–L582, 2001.
20. Lee JM, Zipfel GJ, and Choi DW. The changing landscape of ischaemic brain injury mechanisms. *Nature* 399 (6738 Suppl): A7–A14, 1999.
21. Li Y, Huang T-T, Carlson EJ, Melov S, Ursell PC, Olson JL, Noble LJ, Yoshimura MP, Berger C, Chan PH, Wallace DC, and Epstein CJ. Dilated cardiomyopathy and neonatal lethality in mutant mice lacking manganese superoxide dismutase. *Nat Genet* 11: 376–381, 1995.
22. Lithgow T. Targeting of proteins to mitochondria. *FEBS Lett* 476: 22–26, 2000.
23. Majima HJ, Oberley TD, Furukawa K, Mattson MP, Yen HC, Szweda LI, and St. Clair DK. Prevention of mitochondrial injury by manganese superoxide dismutase reveals a primary mechanism for alkaline-induced cell death. *J Biol Chem* 273: 8217–8224, 1998.
24. Mattson MP. Apoptosis in neurodegenerative disorders. *Nat Rev Mol Cell Biol* 1: 120–129, 2000.
25. Mattson MP, Duan W, Pedersen WA, and Culmsee C. Neurodegenerative disorders and ischemic brain diseases. *Apoptosis* 6: 69–81, 2001.
26. Mihara T and Onuma T. Cytoplasmic chaperons in precursor targeting to mitochondria: the role of MSF and hsp70. *Trends Cell Biol* 6: 104–108, 1996.
27. Motoori S, Majima HJ, Ebara M, Kato H, Hirai F, Kakinuma S, Yamaguchi C, Ozawa T, Nagano T, Tsujii H, and Saisho H. Overexpression of mitochondrial manganese superoxide dismutase protects against radiation-induced cell death in the human hepatocellular carcinoma cell line HLE. *Cancer Res* 61: 5382–5388, 2001.
28. Nishi Y, Haji M, Takayanagi R, Iguchi H, Shimazoe T, Hirata J, and Nawata H. Establishment of characterization of PTHrP-producing human pancreatic cancer cell line. *Int J Oncol* 5: 33–39, 1994.
29. O'Donovan DJ, Katkin JP, Tamura T, Husser R, Xu X, Smith CV, and Welty SE. Gene transfer of mitochondrially targeted glutathione reductase protects H441 cells from *t*-butyl hydroperoxide-induced oxidant stresses. *Am J Respir Cell Mol Biol* 20: 256–263, 1999.
30. Riley PA. Free radicals in biology: oxidative stress and the effects of ionizing radiation. *Int J Radiat Biol* 65: 27–33, 1994.
31. Rofstad EK. Microenvironment-induced cancer metastasis. *Int J Radiat Biol* 76: 589–605, 2000.
32. St Clair DK, Oberley TD, and Ho Y-S. Overproduction of human Mn-superoxide dismutase modulates paraquat-mediated toxicity in mammalian cells. *FEBS Lett* 293: 199–203, 1991.
33. St. Clair DK, Wan XS, Oberley TD, Muse KE, and St Clair WH. Suppression of radiation-induced neoplastic transformation by overexpression of mitochondrial superoxide dismutase. *Mol Carcinog* 6: 238–242, 1992.
34. St Clair DK, Jordan JA, Wan S, and Gairola CG. Protective role of manganese superoxide dismutase against cigarette smoke-induced cytotoxicity. *J Toxicol Environ Health* 43: 239–249, 1994.
35. Sun J, Chen Y, Li M, and Ge Z. Role of antioxidant enzymes on ionizing radiation resistance. *Free Radic Biol Med* 24: 586–593, 1998.
36. Takeshige K and Minakami S. NADH- and NADPH-dependent formation of superoxide anions by bovine heart submitochondrial particles and NADH-ubiquinone reductase preparation. *Biochem J* 180: 129–135, 1979.
37. Tamura T, McMicken HW, Smith CV, and Hansen TN. Mitochondrial targeting of glutathione reductase requires a leader sequence. *Biochem Biophys Res Commun* 222: 659–663, 1996.

38. Tamura T, McMicken HW, Smith CV, and Hansen TN. Gene structure for mouse glutathione reductase, including a putative mitochondrial targeting signal. *Biochem Biophys Res Commun* 237: 419–422, 1997.
39. Thomlinson RH and Gray LH. The histological structure of some human lung cancers and the possible implications for radiotherapy. *Br J Cancer* 9: 539–549, 1955.
40. Toyokuni S, Miyake N, Hiai H, Hagiwara M, Kawakishi S, Osawa T, and Uchida K. The monoclonal antibody specific for the 4-hydroxy-2-nonenal histidine adduct. *FEBS Lett* 359: 189–191, 1995.
41. van Loon APGM, Pesold-Hurt B, and Schatz G. A yeast mutant lacking mitochondrial manganese-superoxide dismutase is hypersensitive to oxygen. *Proc Natl Acad Sci U S A* 83: 3820–3824, 1986.
42. van Putten LM. Tumor reoxygenation during fractionated radiotherapy: studies with a transplantable osteosarcoma. *Eur J Cancer* 4: 173–182, 1968.
43. Wallace DC. Mitochondrial DNA in aging and disease. *Sci Am* 277: 40–47, 1997.
44. Weisiger RA and Fridovich I. Mitochondrial superoxide disimutase. Site of synthesis and intramitochondrial localization. *J Biol Chem* 248: 4793–4796, 1973.
45. Wispe JR, Warner BB, Clark JC, Dey CR, Neuman J, Glasser SW, Crapo JD, Chang L-Y, and Whitsett JA. Human Mn-superoxide dismutase in pulmonary epithelial cells of transgenic mice confers protection from oxygen injury. *J Biol Chem* 267: 23937–23941, 1992.
46. Wong GH. Protective roles of cytokines against radiation: induction of mitochondrial MnSOD. *Biochim Biophys Acta* 1271: 205–209, 1995.
47. Wong GHW, Elwell JH, Oberley LW, and Goeddel DV. Manganous superoxide dismutase is essential for cellular resistance to cytotoxicity of tumor necrosis factor. *Cell* 58: 923–931, 1989.
48. Yen H-C, Oberley TD, Vichitbandha S, Ho Y-S, and St Clair DK. The protective role of manganese superoxide dismutase against adriamycin-induced acute cardiac toxicity in transgenic mice. *J Clin Invest* 98: 1253–1260, 1996.
49. Yen H-C, Nien C-Y, Majima HJ, Lee C-P, Chen S-Y, Wei J-S, and See L-C. Increase of lipid peroxidation by cisplatin in WI38 cells but in SV40-transformed WI38 cells. *J Biochem Mol Toxicol* 17: 39–46, 2003.
50. Zhou W, Zhang Y, Hosch MS, Lang A, Zwacka RM, and Engelhardt JF. Subcellular site of superoxide dismutase expression differentially controls AP-1 activity and injury in mouse liver following ischemia/reperfusion. *Hepatology* 33: 902–914, 2001.

Address reprint requests to:
Hideyuki J. Majima, D.D.S., Ph.D.
Department of Oncology and Department of Space Environmental Medicine
Kagoshima University Graduate School of Medical and Dental Sciences
Kagoshima 890-8544, Japan

E-mail: hmajima@denta.hal.kagoshima-u.ac.jp

Received for publication October 18, 2003; accepted February 19, 2004.

Evaluation of anti-platelet aggregatory effects of aspirin, cilostazol and ramatroban on platelet-rich plasma and whole blood

Hiroko Kariyazono[a], Kazuo Nakamura[a], Junko Arima[a], Osamu Ayukawa[a], Shunji Onimaru[a], Hiroshi Masuda[b], Yoshifumi Iguro[b], Hideyuki J. Majima[c], Ryuzo Sakata[b] and Katsushi Yamada[a]

To compare property in anti-platelet effects of aspirin (a cyclooxygenase inhibitor), cilostazol (a phosphodiesterase III inhibitor) and ramatroban (a specific thromboxane A_2 receptor antagonist), we measured human platelet-rich plasma (PRP) aggregation induced by adenosine diphosphate (ADP), collagen and arachidonic acid, and whole blood (WB) aggregation induced by ADP. The release of P-selectin, transforming growth factor-beta 1, and the formation of thromboxane A_2 in response to agonists were also investigated. Inhibitory effects of 100 μmol/l aspirin, 10 μmol/l cilostazol and 1 μmol/l ramatroban on 5 μmol/l ADP-induced PRP aggregation were similar. However, aspirin strongly inhibited thromboxane A_2 formation in response to 5 μmol/l ADP compared with other drugs. Inhibitory effects of 10 μmol/l cilostazol on PRP aggregation and the release of molecules were quite similar in responsiveness induced by the three agonists. Aspirin and cilostazol inhibited platelet aggregation in a concentration-dependent, non-linear fashion, while ramatroban inhibited linearly with increasing concentration. Anti-platelet effects of drugs having different pharmacological mechanisms were demonstrated clearly by measuring PRP aggregation induced by the three agonists, and by measuring WB aggregation that most probably reflects not only platelet–platelet interactions, but also platelet–leukocyte interactions, as well as the release of intraplatelet molecules. *Blood Coagul Fibrinolysis* **15:157–167 © 2004 Lippincott Williams & Wilkins.**

Blood Coagulation and Fibrinolysis 2004, 15:157–167

Keywords: whole blood aggregation, platelet-rich plasma, aspirin, cilostazol, ramatroban

[a]Department of Clinical Pharmacy and Pharmacology, [b]Department of Thoracic Cardiovascular Surgery, Hepato-Biliary-Pancreatic Surgery, and [c]Department of Oncology, Division of Maxillofacial Radiology and Department of Space Environmental Medicine, Graduate School of Medical and Dental Sciences, Kagoshima University, Kagoshima, Japan.

Sponsorship: This study was supported in part by grant-in-aid for scientific research 13672395 from the Ministry of Education, Culture, Sports, Science and Technology, Japan.

Correspondence and requests for reprints to Kazuo Nakamura, Department of Clinical Pharmacy and Pharmacology, Graduate School of Medical and Dental Sciences, Kagoshima University 8-35-1 Sakuragaoka, Kagoshima 890-8520, Japan.
Tel: +81 99 275 5542; fax: +81 99 265 5293;
e-mail: knaka@denta.hal.kagoshima-u.ac.jp

Received 28 January 2003 **Revised** 26 August 2003
Accepted 4 November 2003

Introduction

Anti-platelet drugs are administered to prevent the formation of thrombus due to platelet activation in patients with myocardial infarction, thrombotic strokes and peripheral vascular disease [1,2]. It is necessary to manage the effects of anti-platelet drugs to within an appropriate therapeutic range to protect patients from the formation of thrombus and bleeding. Measurement of platelet aggregation has been widely carried out to assess platelet function and the effects of anti-platelet drugs. By far the most common method to detect platelet aggregation is by measuring light transmission of platelet-rich plasma (PRP) [3], while another method to detect platelet aggregates in PRP is a light-scattering method based on a particle counting [4,5]. There are also some methods using whole blood (WB) such as electrical impedance aggregometry [6,7], measurement of closure time of an artificial vessel with a bioactive membrane having a microscopic aperture [3,8], light absorbance measurement of blood samples based on agglutination of platelets to fibrinogen-coated beads [3,9,10], and a screen filtration pressure method that measures platelet aggregation in terms of increasing resistance of WB sample flow through a microsieve [11,12]. Notably, the screen filtration pressure method has not been widely utilized to date, largely due to the difficulty of measurement of screen filtration pressure, causing problems with reproducibility and difficulty in the measurement of platelet aggregation. Platelet aggregation is probably mediated by platelet–leukocyte interactions regulated by chemical mediators from leukocytes, erythrocytes and other cells [13,14]. Therefore, it is believed that platelet aggregation in WB could possibly reflect physiological conditions more accurately than aggregation in PRP. Recently, a new type of WB aggregometer with a screen filtration

0957–5235 © 2004 Lippincott Williams & Wilkins

DOI: 10.1097/01.mbc.0000114383.15192.ee

pressure method has been developed; there are some reports regarding this device [15–17].

We have been evaluating *in vitro* anti-platelet effects of the drugs sarpogrelate hydrochloride (a 5-HT_2-serotonergic receptor antagonist) and cilostazol (a phosphodiesterase III inhibitor) [18,19] as well as the clinical usefulness of anti-platelet drugs in patients who underwent mechanical prosthetic valve replacement or arteriosclerosis obliterans [20,21] by measuring PRP aggregability. In our previous reports, anti-platelet drugs inhibited the release of intraplatelet substances such as platelet-derived growth factor [22,23] and transforming growth factor-beta 1 (TGF-β1) [24], which are both contained in the α-granules in resting platelets, and serotonin accompanied with aggregation [18,19].

In the present study, we evaluated the anti-platelet effects of aspirin, cilostazol and ramatroban, a specific thromboxane A_2 (TXA_2) receptor antagonist, on platelet aggregation by measuring both PRP aggregation using the turbidimetric method and WB aggregation using the newly developed screen filtration pressure method, and examined the accuracy of this device by comparing results with PRP aggregation data. We also investigated the release of P-selectin, a platelet α-granule membrane protein [25–27], and TGF-β1 and the formation of TXA_2 in response to platelet agonists as means to evaluate the anti-platelet effects of drugs. Furthermore, detection of platelet–leukocyte interaction in WB aggregometry was examined.

Materials and methods

Reagents

Adenosine diphosphate (ADP) (Sigma, St Louis, Missouri, USA), collagen (General Reagent Collagen Horse Tendon, Hormon-Chemie Co., Ltd., Munich, Germany) and arachidonic acid (Nacalai Tesque, Kyoto, Japan) were used as platelet agonists. Final concentrations of the respective agonists were as follows: ADP, 1, 2, 4, 5 and 8 μmol/l; collagen, 1 μg/ml; and arachidonic acid, 3 mmol/l, as previously described [27,28]. Aspirin was purchased from Sigma. Cilostazol and ramatroban were kindly supplied by Otsuka Pharmaceutical Co., Ltd (Tokushima, Japan) and Bayer AG (Wuppertal, Germany), respectively. Aspirin and ramatroban were dissolved in ethanol and then diluted with saline. Cilostazol was dissolved in *N,N*-dimethylformamide (Nacalai Tesque). Fluorescein isothiocyanate (FITC)-conjugated monoclonal antibody, anti-CD45 and phycoerythrin (PE)-conjugated monoclonal antibody, anti-CD42b, were purchased from Becton Dickinson Pharmingen (San Jose, California, USA).

Preparation of blood sample

Blood samples were collected from healthy volunteers into plastic syringes containing 3.8% sodium citrate (1 : 9). An automatic blood cell counter (Sysmex K-2000; Sysmex, Kobe, Japan) was used to count platelets. In eight healthy volunteers, the mean value of platelet count in WB was $(25.0 \pm 5.0) \times 10^4$ cells/μl. PRP (3×10^5 platelets/μl) and platelet-poor plasma were prepared as previously reported [27,28]. Aliquots of WB and PRP were mixed with a working solution of aspirin and ramatroban (19 : 1), or mixed with a working solution of cilostazol (1 : 399), and then incubated for 3 min at room temperature (23–26°C). Control WB and PRP were mixed with vehicle and incubated similarly. Thus, the final concentrations of ethanol and *N,N*-dimethylformamide were 0.025 and 0.05%, respectively. All subjects were given an explanation of the purpose and design of the study, and consented to donate blood.

Estimation of drug effects on PRP aggregation

PRP obtained 60 min after blood collection was incubated with aspirin, cilostazol or ramatroban at room temperature for 3 min, and then stimulated by ADP (1, 2, 4, 5 and 8 μmol/l), collagen (1 μg/ml) and arachidonic acid (3 mmol/l). PRP aggregation was measured with the turbidimetric method [29], using a Hematracer 801 (M.C. Medical, Tokyo, Japan), and quantified by light transmission as previously reported [27,28]. Effects of drugs on PRP aggregation were estimated by percent maximum aggregation (MA).

Determination of soluble P-selectin, TGF-β1 and thromboxane B_2

PRP samples after measurement of platelet aggregation were centrifuged at $2190 \times g$ for 20 min, and the supernatant was collected to determine the levels of soluble P-selectin (sP-selectin), TGF-β1, and thromboxane B_2 (TXB_2), which is a metabolic product of arachidonic acid and is rapidly formed from TXA_2 but has no biological activity. Samples were stored at −30°C until analysis. The enzyme-linked immunosorbent assay (ELISA) kit for sP-selectin was obtained from Bender MedSystems (Vienna, Austria), the TGF-β1 ELISA kit from R&D Systems, Inc. (Minneapolis, Minnesota, USA) and the TXB_2 ELISA kit from PerSeptive Biosystems (Framingham, Massachusetts, USA).

Measurement of WB aggregation

WB aggregation was measured by a WB aggregometer with the screen filtration pressure method (M.C. Medical). Two hundred microlitres each of WB samples in four reaction tubes was stirred with stirrer bar at 37°C, and pre-incubated for 1 min, followed by the addition of 22 μl each of 1, 2, 4 and 8 μmol/l ADP. Five minutes later, WB samples were sucked to detect aggregation pressure at a rate of 200 μl/6.4 s using a syringe containing screen microsieves made of nickel, 3.7 mm in diameter, with 300 openings of 30×30 μm^2 in a 1-mm-

diameter area. The final platelet aggregation pressure of each reaction tube was determined as the pressure rate of a pressure sensor connected to the syringe. The pressure rate was standardized by a grading curve; 1, 2, 4 and 8 μmol/l ADP were plotted on the *x* axis and the pressure rates (%) were plotted on the *y* axis. Figure 1 shows a representative analysis of platelet aggregation by the WB aggregometer using a grading curve. The concentration of ADP inducing a 50% pressure rate was calculated and indicated as the platelet aggregatory threshold index (PATI). PATI values were used to evaluate WB aggregation.

Time course change in the PATI after blood collection and reproducibility in WB aggregation

To investigate changes in the PATI after blood collection over time, WB aggregation was measured at 5, 15, 30, 60 and 120 min after blood collection in eight healthy volunteers. The reproducibility of WB aggregation was also examined in blood samples. At 60 min after blood collection, the PATI values determined from WB on one day were compared with values from another day when the same measurements were performed.

Fig. 1

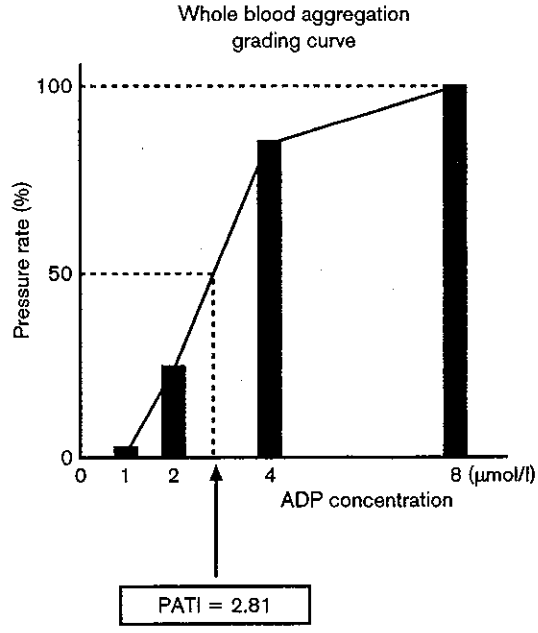

A representative analysis of whole blood aggregation using a grading curve. The *x* axis is adenosine diphosphate (ADP) concentration, and the *y* axis is pressure rate (%). The concentration of ADP inducing 50% pressure rate was calculated and indicated as a platelet aggregatory threshold index value. Whole blood aggregation was measured at 60 min after blood collection. PATI, platelet aggregatory threshold index.

Estimation of drug effects on WB aggregation and its comparison with PRP aggregation

At 60 min after blood collection, the working solutions of aspirin, cilostazol and ramatroban were added to WB, followed by incubation for 3 min. Drug-treated WB was stimulated by ADP and WB aggregation was measured as already described. In addition, PATI values in PRP aggregation were also calculated from light transmission 5 min after ADP addition in a similar manner to WB (Fig. 2), and were compared with those in WB aggregation.

Co-existence of platelets and leukocytes on the microsieve

To investigate the co-existence of platelets and leukocytes on the microsieve after WB aggregometry, staining of platelets and leukocytes was performed by use of dual-colour immunofluorescence. Erythrocytes on the microsieve were lysed with lysis buffer containing NH_4Cl, $NaHCO_3$ and EDTA2Na, and then were fixed with commercially available solution (Cell Fix; Becton Dickinson, San Jose, California, USA). After being washed three times, the microsieves were pre-incubated with 5% bovine serum albumin in phosphate-buffered saline (pH 7.4) at room temperature. After removing the solution, the microsieves were incubated with saturating concentrations of PE-conjugated anti-CD42b and FITC-conjugated anti-CD45 in a total volume of 500 μl phosphate-buffered saline containing 2% bovine serum albumin for 4 h at 4°C in the dark, then washed five times with phosphate-buffered saline. Images of the immunofluorescent samples were obtained using a CSU-10 confocal laser scanning unit (Yokogawa Electric Co., Tokyo, Japan) coupled to an IX90 inverted microscope with UPlanAPO × 20 objective lens (Olympus Optical Co., Tokyo, Japan) and a C5810-01 colour chilled 3CCD camera (Hamamatsu Photonics K. K., Hamamatsu, Japan) [30,31].

Statistical analysis

The data are expressed as means ± standard deviation. Statistical analysis was performed by a one-way analysis of variance, which was followed by Fisher's protected least significant difference test. Relationships between independent variables were assessed by Pearson's correlation. Differences were considered to be significant at $P < 0.05$. StatView J-4.5 software (Abacus Concepts Inc., Berkeley, California, USA) was employed for all calculations.

Results

Inhibitory effects of aspirin, cilostazol and ramatroban on PRP aggregation

MA values from control PRP in response to ADP (1 and 5 μmol/l), collagen (1 μg/ml) and arachidonic acid (3 mmol/l) are presented in Table 1. When control PRP was stimulated by 1 μmol/l ADP, primary aggregation was induced in all specimens, with MAs of 40% or less,

Fig. 2

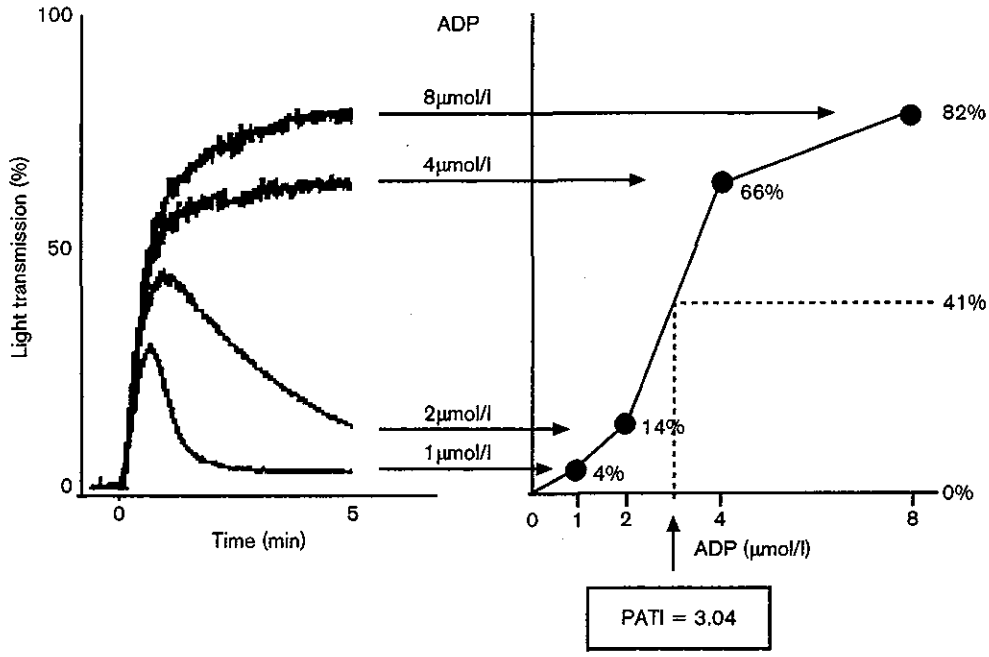

Representation of platelet-rich plasma (PRP) aggregation using the platelet aggregatory threshold index (PATI) value. Left panel shows a representative PRP aggregation by the turbidimetric method. When light transmission 5 min after adenosine diphosphate (ADP) addition is plotted on the grading curve (right panel) and the maximum light transmission value (82%) with 8 μmol/l ADP-induced aggregation is regarded as 100%, the PATI value is calculated as the concentration of ADP causing a 50% light transmission (i.e. 41%) on the grading curve.

Table 1 Circulating plasma levels of sP-selectin, transforming growth factor-beta 1 (TGF-β1) and thromboxane B_2 (TXB_2) and platelet responses in control platelet-rich plasma after stimulation by agonists

		Agonists			
	Circulating plasma levels	ADP 1 μmol/l	ADP 5 μmol/l	Collagen 1 μg/ml	Arachidonic acid 3 mmol/l
MA (%)		36 ± 4	82 ± 2*	84 ± 4*	85 ± 4*
sP-selectin (ng/ml)	98 ± 16	129 ± 9	228 ± 22*	288 ± 29*	239 ± 32*
TGF-β1 (ng/ml)	2.5 ± 0.8	8.8 ± 2.3	28.5 ± 4.2*	38.3 ± 5.6*	47.9 ± 7.0*
TXB_2 (ng/ml)	1.2 ± 0.4	5.5 ± 2.6	54.7 ± 16.7*	249.8 ± 34.0*	478.4 ± 90.8*

Data represent mean ± standard deviation ($n = 8$). MA, percentage maximum aggregation; sP-selectin, soluble P-selectin. *$P < 0.01$ versus the value in response to 1 μmol/l adenosine diphosphate (ADP) (Fisher's protected least significant difference test).

while strong aggregation with MAs of 78% or more was seen in response to 5 μmol/l ADP, collagen and arachidonic acid.

The inhibitory effects of aspirin, cilostazol and ramatroban on PRP aggregation induced by ADP (5 μmol/l), collagen and arachidonic acid were examined. Inhibitory effects of these drugs increased in a concentration-dependent manner (data not shown). As shown in Figure 3a, the percentage decreases in MA values of aspirin at 100 μmol/l, cilostazol at 10 μmol/l and ramatroban at 1 μmol/l after stimulation by ADP were 34, 34 and 33%, respectively. As shown in Figure 3b, the percentage changes in MA after stimulation by collagen were 77% with 100 μmol/l aspirin, 35% with 10 μmol/l cilostazol and 65% with 1 μmol/l ramatroban, respectively. Percentage decrease in MA of 100 μmol/l aspirin, 10 μmol/l cilostazol and 1 μmol/l ramatroban, in response to arachidonic acid, were 83, 38 and 71%, respectively (Fig. 3c).

Inhibitory effects of aspirin, cilostazol and ramatroban on the release of intraplatelet substances

The levels of sP-selectin, TGF-β1 and TXA_2 from control PRP in response to ADP, collagen and arachidonic acid are presented in Table 1. When control PRP

Fig. 3

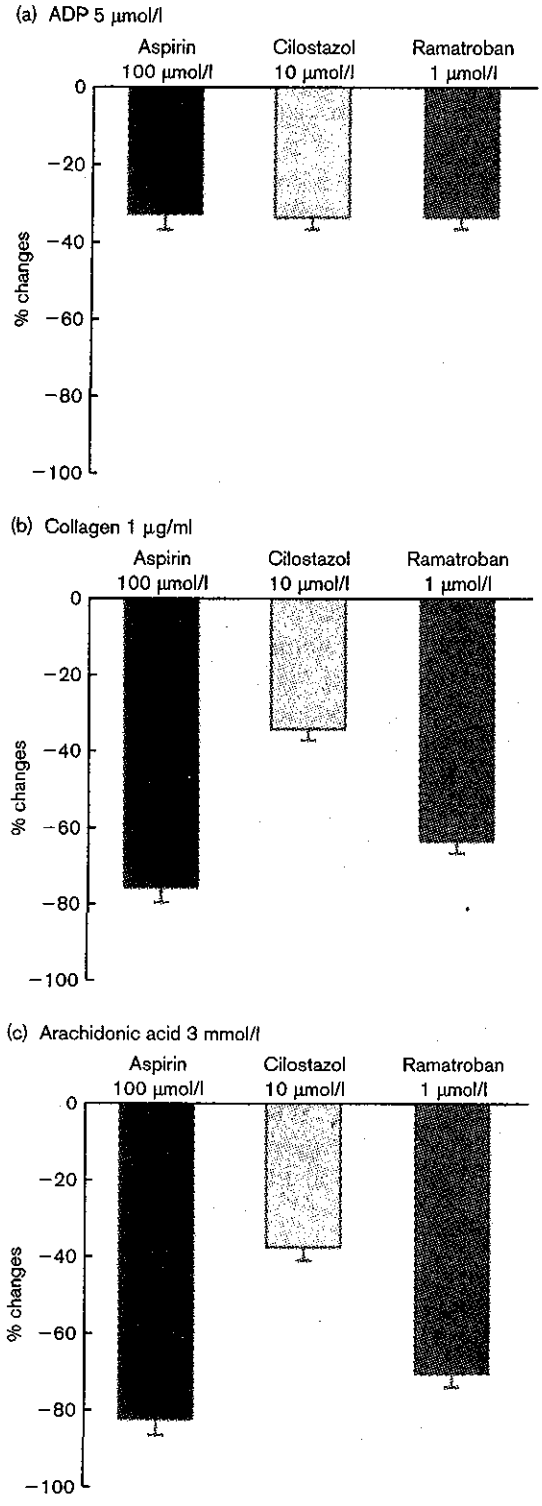

Inhibitory effects of aspirin, cilostazol and ramatroban on platelet-rich plasma (PRP) aggregation induced by (a) adenosine diphosphate (ADP) (5 μmol/l), (b) collagen (1 μg/ml) and (c) arachidonic acid (3 mmol/l). PRP samples were pre-incubated with drugs for 3 min prior to the addition of agonists. Effects of drugs were evaluated as percentage changes in maximum aggregation against vehicle-treated samples. Data represent mean ± standard deviation ($n = 8$).

was stimulated by 1 μmol/l ADP, sP-selectin and TGF-β1 levels increased significantly compared with their circulating plasma levels ($P < 0.05$). TXB_2 also showed high levels, although no difference was found between the levels in response to 1 μmol/l ADP and the levels in circulating plasma. The levels of sP-selectin, TGF-β1 and TXB_2 in response to 5 μmol/l ADP, collagen (1 μg/ml) and arachidonic acid (3 mmol/l) were significantly higher than those in response to 1 μmol/l ADP ($P < 0.001$). Furthermore, TXB_2 levels in response to arachidonic acid markedly increased compared with those in response to 5 μmol/l ADP ($P < 0.001$).

The inhibitory effects of aspirin, cilostazol and ramatroban on the release of P-selectin, TGF-β1 and TXA_2 from platelets in response to ADP (5 μmol/l), collagen and arachidonic acid are shown in Figure 4. When PRP was stimulated by ADP (5 μmol/l), 100 μmol/l aspirin significantly inhibited the release of TXA_2 compared with that of P-selectin and TGF-β1. In contrast, inhibitory effects of 10 μmol/l cilostazol and 1 μmol/l ramatroban on the release of TXA_2 in response to ADP (5 μmol/l) were similar to those on the release of P-selectin and TGF-β1. Aspirin and ramatroban markedly inhibited the release of P-selectin, TGF-β1 and TXA_2 to a similar degree in response to collagen and arachidonic acid. However, 10 μmol/l cilostazol inhibited the release of the three molecules in response to ADP, collagen and arachidonic acid to a similar degree.

Time-dependent change after blood collection and reproducibility in WB aggregation

In order to investigate the relationship between ADP concentration and pressure rate, WB aggregation induced by 1, 2, 4 and 8 μmol/l ADP was measured. As shown in Figure 5a, when control WB and aspirin-treated (10, 50, 100 and 500 μmol/l) WB were stimulated by ADP, the pressure rates in all samples increased depending on ADP concentrations. These data were presented as the dose–response plots for aspirin concentrations in Figure 5b. PATI values elevated with the increase in aspirin concentration. Figure 6 shows time-dependent changes in the PATI values after blood collection. PATI values immediately after blood collection (5 min) were 5.68 ± 1.71, and decreased gradually until 60 min after blood collection, and then increased slightly after 120 min. The following experiments to evaluate WB aggregation were performed using blood samples 60 min after collection. In the examination of reproducibility between two different sample days, the mean values of PATI from the same volunteers were 2.63 ± 0.65 and 2.52 ± 0.84 ($n = 8$), respectively, and no significant difference in PATI values between the two days was observed. While platelet counts from eight volunteers ranged from 17.5×10^4 to 31.2×10^4 cells/μl [mean platelet count, $(25.0 \pm 5.0) \times 10^4$ cells/μl], PATI values were in

Fig. 4

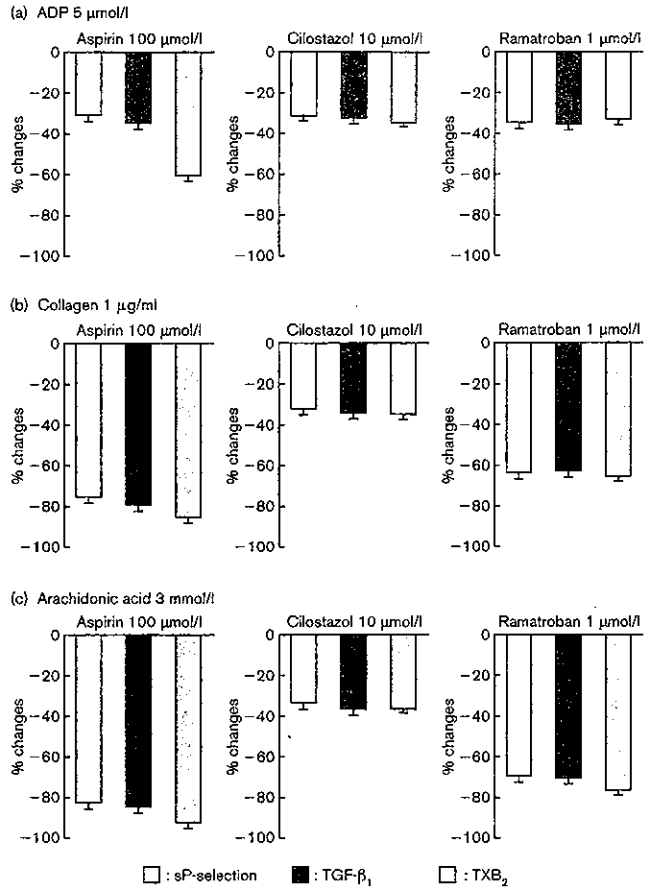

Inhibitory effects of aspirin, cilostazol and ramatroban on release reaction in response to (a) adenosine diphosphate (ADP), (b) collagen and (c) arachidonic acid. Platelet-rich plasma (PRP) samples were pre-incubated with drugs for 3 min prior to the addition of ADP (5 μmol/l), collagen (1 μg/ml) and arachidonic acid (3 mmol/l). Levels of soluble P-selectin (sP-selectin), transforming growth factor-beta 1 (TGF-β1) and thromboxane B_2 (TXB_2) were measured as described in Materials and methods. Effects of drugs on each parameter were evaluated as percentage changes against vehicle-treated samples. Data represent mean ± standard deviation ($n = 8$).

the range of 2.28–3.87 μmol/l (mean, 2.98 ± 0.52 μmol/l). There was no correlation between platelet counts and PATI values.

Inhibitory effects of aspirin, cilostazol and ramatroban on WB and PRP aggregation induced by ADP (1, 2, 4 and 8 μmol/l)

When aspirin-treated, cilostazol-treated and ramatroban-treated WB were stimulated by ADP (1, 2, 4 and 8 μmol/l), the PATI values increased depending upon concentration of the respective drugs, reaching 7.15 ± 0.70 with 500 μmol/l aspirin, 7.33 ± 0.86 with 50 μmol/l cilostazol and 7.91 ± 0.18 with 10 μmol/l ramatroban. Next, these changes in PATI values on WB aggregation were compared with those on PRP aggregation induced by same concentration of ADP. The PATI values from drug-treated PRP also elevated in a concentration-dependent manner, reaching 5.50 ± 1.86 with 500 μmol/l aspirin, 7.36 ± 0.89 with 50 μmol/l cilostazol and 4.53 ± 0.50 with 10 μmol/l ramatroban. Inhibitory effects of aspirin, cilostazol and ramatroban on both WB and PRP aggregation were expressed as the percent increase of PATI values against control samples. As shown in Figure 7, increases of PATI by aspirin and cilostazol on both WB and PRP aggregation were found to be non-linear. In contrast, ramatroban resulted in the increase of PATI in a linear fashion. Cilostazol showed a steep increase of PATI in PRP compared with that in WB.

Confocal scanning laser microscopy

Figure 8 shows representative confocal and fluorescent images of platelets and leukocytes on the microsieve. When WB was stimulated by ADP (8 μmol/l), aggregates were observed on the microsieve in the confocal mode (Fig. 8a). In the same visual field as Figure 8a, platelets stained with PE-conjugated anti-CD42b showed red fluorescence (Fig. 8b), and leukocytes stained with FITC-conjugated anti-CD45 showed green fluorescence (Fig. 8c). Figure 8d indicates the co-existence of platelets and leukocytes.

Correlations between independent variables

The pressure rates of WB aggregation in aspirin-treated WB samples in response to ADP (1, 2, 4 and 8 μmol/l) were compared with the maximum aggregation rates of PRP aggregation and the released levels of sP-selectin, TGF-β1 and TXA_2 in aspirin-treated PRP samples stimulated by ADP (1, 2, 4 and 8 μmol/l). Correlation analysis was carried out between independent variables in aspirin-treated, cilostazol-treated, or ramatroban-treated WB and PRP samples in response to ADP (1, 2, 4 and 8 μmol/l). Close correlations were found between the pressure rate in WB aggregometry and other variables from PRP aggregometry, and between the PATI values from WB and PRP aggregation (Table 2).

Discussion

In the present study, we first examined the effects of aspirin, cilostazol and ramatroban on PRP aggregation induced by ADP (5 μmol/l), collagen (1 μg/ml) and arachidonic acid (3 mmol/l). The drugs inhibited PRP aggregation induced by ADP (5 μmol/l) in a concentration-dependent manner, and the effects of aspirin with 100 μmol/l, cilostazol with 10 μmol/l and ramatroban with 1 μmol/l were similar, showing an approximate 35% decrease in MA. Inhibitory effects of aspirin and ramatroban at these concentrations on collagen-induced and arachidonic acid-induced aggregation were stronger than those on ADP-induced aggregation. In contrast, inhibitory effects of 10 μmol/l cilostazol were similar in responsiveness when induced by the three agonists. The effects of ADP on platelets are mediated by at

Fig. 5

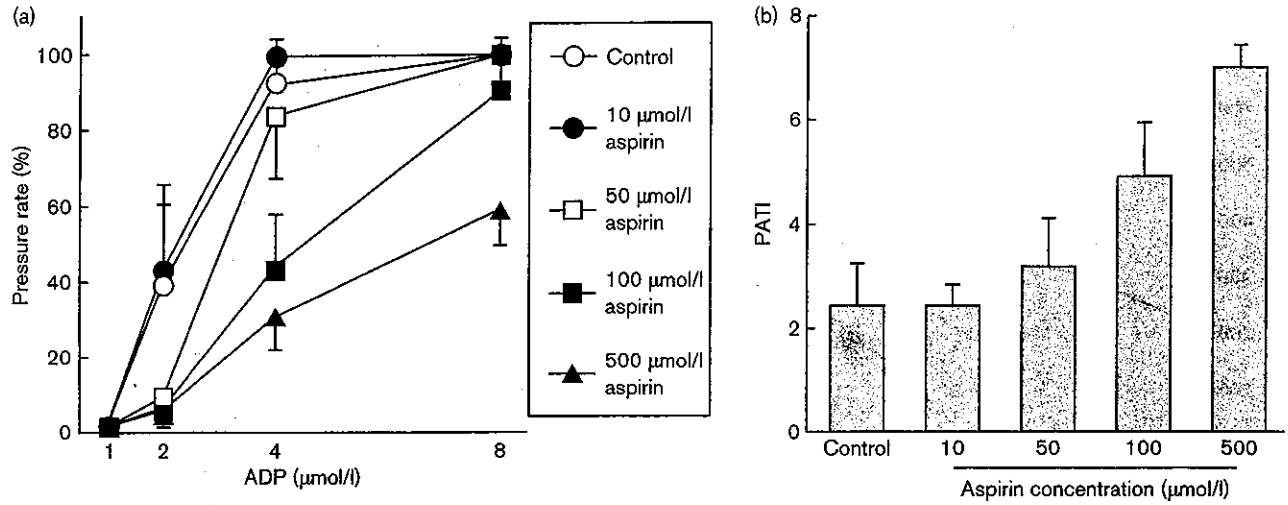

Relationship between adenosine diphosphate (ADP) concentration and pressure rate (%) in whole blood aggregation. Whole blood was pre-incubated with or without aspirin for 3 min prior to the addition of ADP (1, 2, 4 and 8 μmol/l). Whole blood aggregation was measured at 60 min after blood collection. Data represent mean ± standard deviation ($n = 8$). PATI, platelet aggregatory threshold index.

Fig. 6

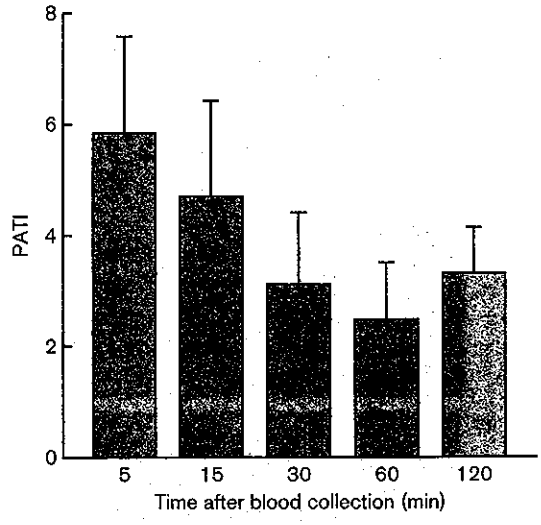

Time-dependent changes in platelet aggregatory threshold index (PATI) values after blood collection. Whole blood was stimulated by adenosine diphosphate (ADP) (1, 2, 4 and 8 μmol/l), and whole blood aggregation was measured at 5, 15, 30, 60 and 120 min after blood collection and PATI values were obtained. Data represent mean ± standard deviation ($n = 8$).

least three receptors; the P2X receptor that mediates rapid Ca ion influx, the P2Y1 receptor coupled to Gq-protein that stimulates phospholipase C (PLC) and induces shape change, and the P2TAC receptor coupled to the Gi-protein that inhibits adenylyl cyclase [32]. Since aspirin inhibited ADP-induced PRP aggregation to a certain degree in the present study, aspirin, a cyclooxygenase inhibitor, may cause the inhibition of PRP aggregation in response to ADP through the P2Y1 receptor. The effects of aspirin on platelet aggregation in response to collagen may be due to the inhibition of platelet activation via glycoprotein (GP) Ia/IIa (the $\alpha_2\beta_1$ integrin), CD36 (GPIV, also known as GPIIIb), or GPVI, which are collagen receptors and lead to PLCγ2 tyrosine phosphorylation and bring about TXA_2 formation [33]. GPIV may accelerate the rate of adhesion once platelets establish contact with collagen fibres via GPVI and GPIa/IIa [34]. Aspirin markedly inhibits PRP aggregation in response to arachidonic acid, because arachidonic acid is utilized in TXA_2 formation.

Next, we measured the levels of sP-selectin, TGF-β1 and TXB_2 in response to ADP, collagen and arachidonic acid. Aspirin markedly decreased TXB_2 levels compared with levels of sP-selectin and TGF-β1 in response to ADP. In contrast, the rates of decrease of TXB_2 by cilostazol and ramatroban were similar to those of sP-selectin and TGF-β1 in response to ADP. Furthermore, aspirin and ramatroban strongly inhibited the release of P-selectin, TGF-β1 and TXB_2 in response to collagen and arachidonic acid compared with the response induced by ADP. These results suggest that aspirin may inhibit not only TXA_2 formation via cyclooxygenase, but also could inhibit the release reaction of TXA_2 via activation of PLC. Stimulation of platelets by collagen and arachidonic acid induces TXA_2 production and the release reaction of intraplatelet substances. Ramatroban inhibits TXA_2 binding to the TXA_2 receptor on the surface of plate-

Fig. 7

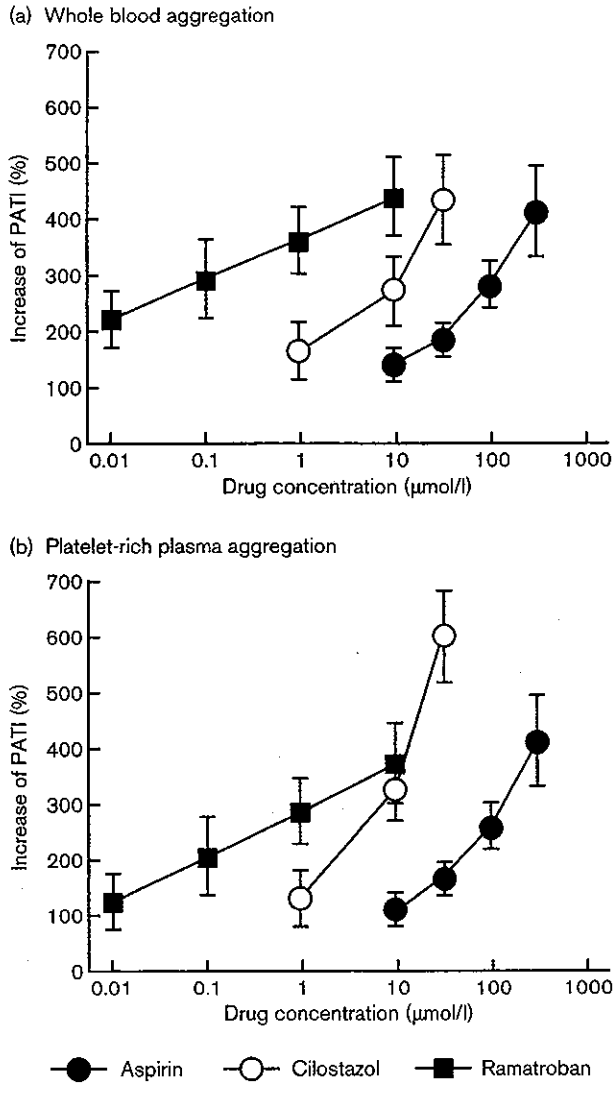

Inhibitory effects of aspirin, cilostazol and ramatroban on (a) whole blood and (b) platelet-rich plasma (PRP) aggregation. Whole blood and PRP samples were pre-incubated with aspirin, cilostazol and ramatroban for 3 min prior to the addition of adenosine diphosphate (ADP) (1, 2, 4 and 8 μmol/l). Percentage changes of platelet aggregatory threshold index (PATI) values for drug-treated samples against those for vehicle-treated samples were plotted along the vertical axis. Data represent mean ± standard deviation ($n = 8$). PATI values from vehicle-treated whole blood aggregation were 1.73 ± 0.30 for ethanol (aspirin and ramatroban) and 2.11 ± 0.70 for *N,N*-dimethylformamide (DMF) (cilostazol). PATI values from vehicle-treated PRP aggregation were 1.31 ± 0.30 for ethanol (aspirin and ramatroban) and 1.25 ± 0.23 for DMF (cilostazol).

lets. Therefore, while both aspirin and ramatroban inhibit the release of P-selectin, TGF-β1 and TXB_2 in response to collagen and arachidonic acid, released levels of TXB_2 in response to ADP are more strongly inhibited by aspirin than ramatroban. Evidence of this may be seen in the report that TXB_2 mediates platelet

Fig. 8

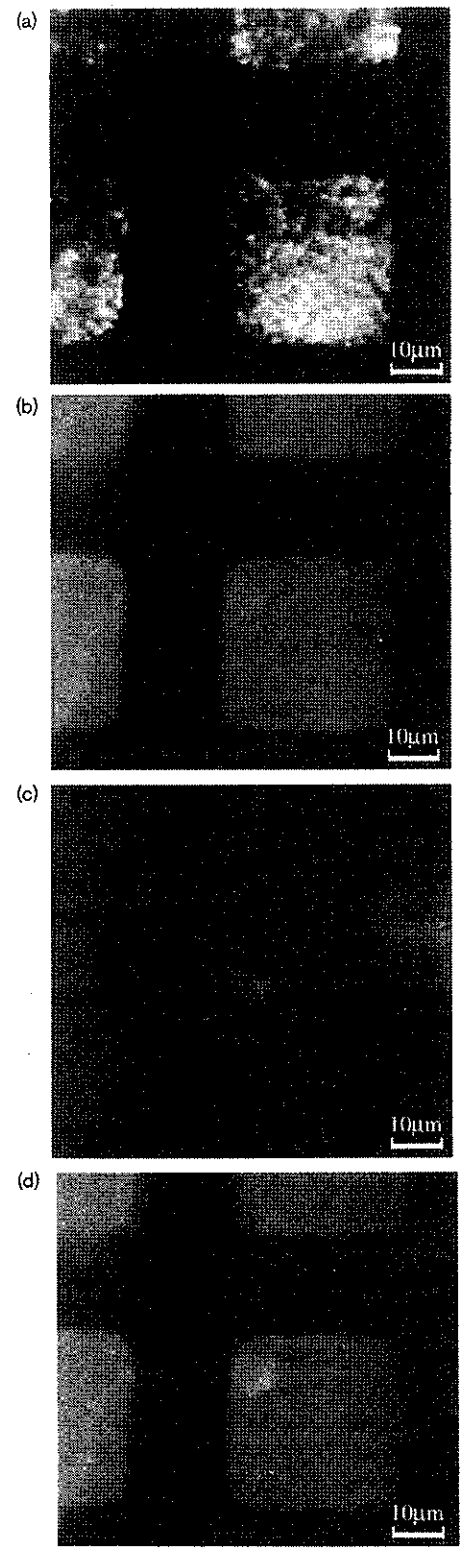

Confocal and fluorescent images of platelets and leukocytes on the microsieve. (a) When whole blood was stimulated by adenosine diphosphate (8 μmol/l), aggregates were observed on the microsieve in the confocal mode. (b), (c) and (d) Images of the fluorescent mode corresponding to the confocal mode.

Table 2 Correlations between pressure rate in whole blood aggregometry and other independent variables from platelet-rich plasma (PRP) aggregometry

	Whole blood:PRP	Coefficients (*R*)	*P* value
Aspirin-treated samples	Pressure rate:MA	0.849	< 0.001
	Pressure rate:sP-selectin	0.897	< 0.001
	Pressure rate:TGF-β1	0.920	< 0.001
	Pressure rate:TXB_2	0.737	< 0.001
	PATI:PATI	0.920	< 0.001
Cilostazol-treated samples	Pressure rate:MA	0.761	< 0.001
	Pressure rate:sP-selectin	0.823	< 0.001
	Pressure rate:TGF-β1	0.766	< 0.001
	Pressure rate:TXB_2	0.785	< 0.001
	PATI:PATI	0.828	< 0.001
Ramatroban-treated samples	Pressure rate:MA	0.638	< 0.001
	Pressure rate:sP-selectin	0.768	< 0.001
	Pressure rate:TGF-β1	0.774	< 0.001
	Pressure rate:TXB_2	0.802	< 0.001
	PATI:PATI	0.894	< 0.001

MA, percentage maximum aggregation; sP-selectin, soluble P-selectin; TGF-β1, transforming growth factor-beta 1; TXB_2, thromboxane B_2; PATI, platelet aggregatory threshold index.

activation through a system linked to PLC [35]. Cilostazol inhibited the release of all the molecules in response to ADP, collagen and arachidonic acid in a similar fashion. These results may be due to the difference in pharmacological mechanisms between aspirin (a cyclooxygenase inhibitor), cilostazol (a phosphodiesterase III inhibitor) and ramatroban (a specific TXA_2 receptor antagonist). Different signal pathways in platelets most surely play important roles in these events.

Third, we examined the effects of these drugs on WB aggregation induced by ADP (1, 2, 4 and 8 μmol/l) using the newly developed WB aggregometer with the screen filtration pressure method, and the results were compared with those from PRP aggregation induced by the same agonist. To measure WB aggregation, some devices such as the PFA-100 [3,8], and the Ultegra Platelet Analyzer [3,9,10] have been developed. In the present study, a WB aggregometer with a microsieve made of nickel, 3.7 mm in diameter, with 300 openings/1 mm diameter area was used [15]. The pressure rate (%) of WB through the microsieve after stimulation by ADP (1, 2, 4 and 8 μmol/l) was measured. Although we did not compare data from this device with another WB aggregometer, it is reported that platelet aggregation data from the PFA-100 and the Ultegra correlated well to data from a four-channel Chrono-log Lumi-Aggregometer using PRP [10]. We obtained the result that the pressure rate (%) of WB through the microsieves and maximum aggregation rate (%) of PRP correlated closely. In addition, there were close correlations between PATI values from WB aggregation and PRP aggregation, and also between the pressure rate (%) of WB and the levels of molecules released from platelets. Therefore, we believe that data from the newly developed WB aggregometer bear a striking resemblance to other devices such as the PFA-100 and the Ultegra. Recently, the effects of anti-platelet drugs were successfully evaluated using the WB aggregometer with the screen filtration pressure method [16]. In the present study, we confirmed a high reproducibility of WB aggregation by this apparatus. On the other hand, the PATI value (which represents the concentration of ADP inducing a 50% pressure rate) was highest at 5 min after blood collection and then gradually decreased up to 60 min time, in accordance with previous reports [15,16]. Thus, the data from the WB aggregometer were variable over the time period studied. Although the reason why the PATI value varies depending on time has not yet been clarified, it is possible that a change in the responsiveness of receptors on blood cells or unstable anti-thrombotic physiological substances such as prostacyclin may be contributing factors [15]. Therefore, in clinical laboratories, it is necessary to decide on the time after blood collection determining WB aggregability in order to obtain accurate results. In addition, it is possible to use this device as a rapid bedside test by measuring immediately after blood collection.

In fact, clinical research on subjects who had taken aspirin for angina pectoris is now being conducted. Addition of ADP to WB samples collected from the patients was performed punctually 60 min after drawing blood. In our unpublished data, PATI values in WB aggregation on the seventh day after cessation of taking aspirin to prevent extra bleeding during surgery of coronary artery bypass grafting were lower than those in the aspirin-taking period (2.19 ± 1.33 versus 4.81 ± 2.03). These results suggest that the WB analyser with screen filtration pressure method is a useful instrument even in clinical aspects to evaluate the anti-platelet effects of drugs, as well as other devices.